# Ring-type multisoliton dynamics in shallow water

Abdul Mannan, Renato Fedele, Miguel Onorato, Sergio De Nicola, and Dušan Jovanović

Phys. Rev. E **91**, 012921 — Published 26 January 2015

DOI: 10.1103/PhysRevE.91.012921

# Ring-type multi-soliton dynamics in shallow water

**Abdul Mannan**,[1,2] **Renato Fedele**,[3,2] **Miguel Onorato**,[4,5]

**Sergio De Nicola**,[6,2] and **Dušan Jovanović**[7,2]

[1]*Dipartimento di Matematica e Fisica,*

*Seconda Università degli Studi di Napoli, Sede di Caserta, Caserta, Italy*

[2]*INFN Sezione di Napoli, Complesso Universitario di M.S. Angelo, Napoli, Italy*

[3]*Dipartimento di Fisica, Università di Napoli Federico II,*

*Complesso Universitario di M.S. Angelo, Napoli, Italy*

[4]*Dipartimento di Fisica, Università di Torino, Torino, Italy*

[5]*INFN Sezione di Torino, Torino, Italy*

[6]*SPIN-CNR, Complesso Universitario di M.S. Angelo, Napoli, Italy*

[7]*Institute of Physics, University of Belgrade, Belgrade, Serbia*

## Abstract

The propagation, in a shallow water, of nonlinear ring waves in the form of multi-solitons is investigated theoretically. This is done by solving both analytically and numerically the *cylindrical* (also referred to as *concentric*) Korteweg-de Vries equation (cKdVE). The latter describes the propagation of weakly nonlinear and weakly dispersive ring waves in an incompressible, inviscid, and irrotational fluid. The spatiotemporal evolution is determined for a cylindrically symmetric response to the *free fall* of an initially given multi-soliton ring. Analytically, localized solutions in the form of *tilted solitons* (see Figures 1-6) are found. They can be thought as single- or multi-ring solitons formed on a conic-modulated water surface, with an oblique asymptote in arbitrary radial direction (*tilted* boundary condition). Conversely, the ring solitons obtained from numerical solutions are localized single- or multi-ring structures (*standard* solitons), whose wings vanish along all radial directions (*standard* boundary conditions). It is found that the wave dynamics of these *standard* ring-type localized structures differs substantially from that of the *tilted* structures. A detailed analysis is performed to determine the main features of both multi-ring localized structures, particularly their break-up, multiplet formation, overlapping of pulses, overcoming of one pulse by another, "amplitude – width" complementarity, etc., that are typically ascribed to a soliton-like behaviour. For all the localized structures investigated, the soliton-like character of the rings is found to be preserved during (almost) entire temporal evolution. Due to their cylindrical character, each ring belonging to one of these multi-ring localized structures experiences the *physiological decay* of the peak and the *physiological increase* of the width, respectively, while propagating ("amplitude – width" complementarity). As in the planar geometry, i.e., planar Korteweg-de Vries equation (pKdVE), we show that, in the case of the tilted analytical solutions, the instantaneous product $P = (maximum\ amplitude) \times (width)^2$ is rigorously constant during all the soliton spatiotemporal evolution. Nevertheless, in the case of the numerical solutions, we show that this product is not preserved, i.e., the instantaneous physiological variations of both peak and width of each ring do not compensate each other as in the tilted analytical case. In fact, the amplitude decay occurs faster than the width increase, so that $P$ decreases in time. This is more evident in the early times than in the asymptotic ones (where actually cKdVE reduces to pKdVE). This is in contrast to previous investigations on the early-time localized solutions of the cKdVE.



PACS numbers: 47.35.Fg, 92.10.Hm, 05.45.-a

## I. INTRODUCTION

The study of nonlinear wave dynamics is ubiquitous nowadays in many areas of physics and with typical dimensions ranging from nano- to astro-physical scales [1–5]. Probably the earliest example, from which most of the well-known nonlinear problems and the related equations have originated, is the surface gravity wave physics in both the shallow and the deep water regimes. At the present time, a large body of nonlinear effects is encountered in disciplines such as nonlinear optics, plasma physics, electrical transmission lines, condensed matter, geophysics, and astrophysics that are fully similar to those discovered previously in water wave physics. It is interesting to observe that several mathematical techniques, used to analyze and solve the nonlinear partial differential equations, have been developed for the first time in water wave physics and, later on, transferred to the other disciplines.

As it has been pointed out in [6], the set of fluid equations that describes the water dynamics appears to be transparent only superficially, because it actually contains a vast diversity of physical phenomena. In different regimes, the appropriate asymptotic expansions and/or approximations give rise to a large variety of nonlinear wave equations, such as Korteweg - de Vries equation (KdVE), nonlinear Schrödinger equation (NLSE) and Kadomtsev - Petviashvili equation (KPE) [1–5, 7], which admit several soliton-like solutions. Later, similar solutions have been derived also in many other disciplines and applied to a number of very different physical problems.

Remarkably, the nonlinear water wave physics is related not only to the naturally occurring extreme events [7, 8], such as the rogue waves [9, 10] and the tsunami generation [11], but it includes also the study of artificially-produced nonlinear wave phenomena [12], relevant to physical oceanography and environmental risk studies [7]. In the present paper, we consider a particularly interesting problem of the water waves generated by the *free fall* of a column of water, initially confined to a finite region on the water surface, which falls down under the action of the gravity. In principle, the initial perturbation of the water elevation (i.e. the initial profile of the column) can be arbitrary, but we confine our attention to those that are cylindrically symmetric with respect to a vertical axis. Therefore, we consider the spatiotemporal evolution of an initially given system of concentric hollow columns of water that have an initial profile of ring solitons. In order to be in a shallow water regime, we consider weakly nonlinear perturbations of the water elevation and the width of each ring

much longer than the unperturbed water depth. Then, the resulting concentric nonlinear wave dynamics that is originated by the free evolution of such an initial structure under the action of the gravity is governed by the concentric (or cylindrical) Korteweg-de Vries equation (cKdVE) [6]. The typical solutions of the latter are the ring-type waves. In this work, we consider a weakly nonlinear spatiotemporal evolution of the initial profiles that correspond either to a single-ring soliton or to several-ring solitons, that hereafter we simply call "multi-ring solitons". This study has been carried out analytically for *tilted* solitons, i.e. for localized structures that "live" on a conic-modulated water surface and possess an oblique asymptote along any radial direction (*tilted* boundary conditions), and numerically for localized structures whose wings vanish asymptotically along any radial direction (*standard* boundary conditions), respectively.

Earlier investigations on cKdVE have been carried mostly in plasmas and only few contributions for shallow water have appeared in the literature till now. The cKdVE has been used to explicate both the observations of the cylindrical ion acoustic solitons [13] and of the soliton propagation in a warm plasma with two ion species [14]. It was observed that, in early times, the solitons in a two ion species plasma are narrower and faster than their counterpart in a single ion plasma and that the break up of an initial disturbance into several solitons is more likely to occur in a multi-ion warm plasma than in a cold single-ion one [14]. Pioneering results on the localized analytical solutions of cKdVE have been presented in [15, 16].

Suitable transformations which reduce the cKdVE to the standard KdVE and vice versa have been discovered by several authors [17–20]. In Ref. [18], such transformation produced solutions in the form of N solitons interacting with each other and moving in a time-dependent and nonuniform background. In Refs. [19, 20], the transformations between the cKdVE and the planar KdVE (pKdVE) [2, 21] have been used to establish a further correspondence between the family of cylindrical nonlinear Schrödinger equations (cNLSEs) and that of cKdVE. Suitable transformations reducing cNLSE to NLSE and vice versa have also been discovered [19, 20, 22].

The propagation and interaction of cylindrical soliton in shallow water of variable depth have been considered in [23]. Given the difficulty to find analytical localized solutions of the cKdVE satisfying standard boundary conditions, an *ad hoc* modified cKdVE which describes the long waves on a beach has been derived. Within this framework, the interaction between

imploding and exploding (i.e., convergent and divergent) waves has also been studied through a pair of *ad hoc* modified cKdVE.

In this paper, we adopt the model of an incompressible, inviscid, irrotational water, described by the set of Euler's fluid equations. In the cylindrical geometry and using a standard multiple scale analysis for weakly nonlinear and dispersive waves, this set of equations is suitably reduced to the cKdVE. In the following sections, we briefly summarize the derivation of the irrotational cKdVE (cylindrically symmetry) and compare it to the standard (i.e., planar) KdVE.

We provide a (1+1)D representation and adopt a pair of spatiotemporal dimensionless coordinates, say $R$ and $T$, that represent the space-like propagation coordinate and the time, respectively [24]. Then, we express these solutions by means of a (2+1)D representation, where $R$ is expressed in terms of the Cartesian horizontal coordinates, say $X$ and $Y$ ($R = \sqrt{X^2 + Y^2}$), while the time-like variable is still $T$ [24].

## II. THE FLUID MODEL ADOPTED

The water is regarded as an incompressible, irrotational, inviscid fluid, with a zero surface tension and with the density $\rho$. It lies on an impermeable bed, with constant depth and with a constant atmospheric pressure at the free surface.

### A. Model Equations

The governing equations in cylindrical symmetry have been derived earlier, and for the details of the procedure we refer the reader to the previous literature (see Refs. [6, 17, 25], and references therein). Below, we present its basic concept.

In cylindrical coordinates $(r, \theta, z)$, with the $z$-axis directed upwards in the vertical direction, the flow region is bounded from below by a solid bottom at $z = 0$, and from above by a free surface. The latter is described by an equation of the type $z = z(r, t)$. The fluid is taken to be unbounded in the radial direction ($0 < r < \infty$). For simplicity, we consider perturbations with a large characteristic length which, at all times, have a fixed vertical axis of symmetry. As a consequence, all quantities are independent of the azimuthal angle

$\theta$ and the perpendicular component of the velocity field, $u_r$, is strictly radial. Our governing equations are, essentially, the Euler's equations of motion and continuity in cylindrical symmetry, viz.,

$$\frac{\partial u_r}{\partial t} + \epsilon \left( u_r \frac{\partial u_r}{\partial r} + w \frac{\partial u_r}{\partial z} \right) = -\frac{\partial p}{\partial r} \,, \tag{1}$$

$$\delta^2 \left[ \frac{\partial w}{\partial t} + \epsilon \left( u_r \frac{\partial w}{\partial r} + w \frac{\partial w}{\partial z} \right) \right] = -\frac{\partial p}{\partial z} \,, \tag{2}$$

$$\frac{\partial u_r}{\partial r} + \frac{1}{r} u_r + \frac{\partial w}{\partial z} = 0 \,, \tag{3}$$

where $z$ has been normalized to the constant unperturbed depth $h_0$; $p$ is the dimensionless pressure, normalized to $\rho g h_0$ (where $g$ is the acceleration of gravity), which measures the deviation from the unperturbed hydrostatic pressure; the radial coordinate $r$ is normalized to the wavelength $\lambda$; $t$ is the time variable normalized to $\lambda/\sqrt{g h_0}$; $u_r$ is the radial velocity component normalized to $\sqrt{g h_0}$; $w$ is the vertical velocity component normalized to $h_0 \sqrt{g h_0}/\lambda$. Boundary conditions are given by

$$p = \eta \;\text{ and }\; w = \frac{\partial \eta}{\partial t} + \epsilon u_r \frac{\partial \eta}{\partial r} \;\text{ on }\; z = 1 + \epsilon \eta \tag{4}$$

and

$$w = 0 \;\text{ on }\; z = 0 \,. \tag{5}$$

Equations (1)-(5) contain two parameters, $\delta$ and $\epsilon$, that fix the relevant scales of the problem. The parameter $\delta \equiv h_0/\lambda$ is the measure of the shallowness of the water. Likewise, the parameter $\epsilon$ is the measure of the nonlinearity (i.e. of the relative scale of the amplitude), defined as $\epsilon = a/h_0$. Here $a$ is the maximum value of the water depth perturbation, say $\Delta h$. These can be used to express an arbitrary perturbation of the water surface as $h(r,t) = h_0 + \Delta h(r,t) = h_0 + a\eta(r,t)$, where $a = \max(\Delta h(r,t))$ and $\eta(r,t)$ is the dimensionless *elevation* of the surface wave, defined as $\eta(r,t) = \Delta h(r,t)/a$.

### B. Cylindrical KdVE

The detailed derivation of the cKdVE is provided in Appendix A. Here, we only briefly describe how it is deduced from the above fluid model [Eqs. (1) – (5)], skipping all the details. Following Refs. [6, 17, 25], introducing the following stretched coordinates $\zeta$ and $s$

$$\zeta = \frac{\epsilon^2}{\delta^2}(r - t), \quad s = \frac{\epsilon^6}{\delta^4} r \,, \tag{6}$$

and using a multiple scale method [6, 17, 25], one can reduce the fluid Eqs. (1) – (5) to the cylindrical (or concentric) Korteweg-de Vries (cKdVE), viz.

$$\frac{\partial H_0}{\partial s} + \frac{3}{2} H_0 \frac{\partial H_0}{\partial \zeta} + \frac{1}{6} \frac{\partial^3 H_0}{\partial \zeta^3} + \frac{H_0}{2s} = 0\,, \tag{7}$$

where $H_0$ is the rescaled leading order term of the elevation expansion, say $\eta_0$ (for details see Ref. [17]). Note that, according to Appendix A, the last term of Eq. (7), i.e., $H_0/2s$ comes from the cylindrical geometry adopted in our description. If we formally remove this term, Eq. (7) reduces to the pKdVE [see Eq. (11)].

We perform the following transformation:

$$\zeta(R,T) = R - T\,, \quad s(R,T) = T\,, \tag{8}$$

with

$$v(R,T) = H_0(\zeta(R,T), s(R,T))\,, \tag{9}$$

where $T$ and $R$ ($0 < T < \infty$, $0 \leq R < \infty$) play the role of the time and the space-like coordinates, the latter conforming to the propagation (or, more precisely, to the expansion) along the radial direction [24], respectively. Using these transformations, we reduce Eq. (7) in the following form:

$$\frac{\partial v}{\partial T} + \frac{\partial v}{\partial R} + \frac{3}{2} v \frac{\partial v}{\partial R} + \frac{1}{6} \frac{\partial^3 v}{\partial R^3} + \frac{v}{2T} = 0\,. \tag{10}$$

These equations yield cylindrical, ring-type, multi-soliton solutions (both analytical and numerical) in the $(R,T)$ domain.

## III. ANALYTICAL SOLUTIONS: TILTED RING-TYPE MULTI-SOLITONS

As it has been demonstrated by several authors [13, 14, 18–20], a class of analytical solutions of the cKdVE (7) can be obtained from the solutions of the pKdVE

$$\frac{\partial u}{\partial \tau} + \frac{3}{2} u \frac{\partial u}{\partial \xi} + \frac{1}{6} \frac{\partial^3 u}{\partial \xi^3} = 0, \tag{11}$$

employing the appropriate transformations of variables. For instance, if $u(\xi,\tau)$ is solution of Eq. (11), then the function

$$H_0(\zeta, s) = s^{-1} \left[ u\left(\xi = s^{-1/2}\zeta, \tau = -2s^{-1/2}\right) + \zeta/3 \right] \tag{12}$$

is solution of Eq. (7) [19, 20]. In particular, different families of soliton solutions of the pKdVE with standard boundary conditions can be exactly transformed into soliton solutions of the cKdVE with *tilted* boundary conditions [19, 20]. By using the transformations (8) and (9), we easily get

$$v\left(R,T\right)=\frac{1}{T}\left[u\left(\frac{R-T}{T^{1/2}},-\frac{2}{T^{1/2}}\right)+\frac{R-T}{3}\right]. \tag{13}$$

Similar transformations have been found also to recast the planar Kadomtsev-Petviashvili equation into its cylindrical counterpart. [26].

If $u$ is a planar one-soliton that satisfies the standard boundary conditions, i.e. $u\left(\xi,\tau\right)\to 0$ when $\xi\to\pm\infty$, Eq. (13) shows clearly that, in the $(R,T)$ domain, $v\left(R,T\right)$ is the superposition of a localized structure and a straight line. The former has the amplitude that decays as $1/T$ and the width that increases as $\sqrt{T}$. The straight line is given by: $R/T-1/3$; then its slope decreases as $1/T$. Consequently, at each $T$, $v\left(R,T\right)$ is a localized structure whose wings fit to the oblique asymptote: $v=R/T-1/3$; then, we refer, $v$ to as *tilted* localized structure because it satisfies the *tilted* boundary conditions. It is worth noting that, for $T\to\infty$, we have $v\to-1/3$, i.e. with the passing of time a tilted soliton gradually flattens, reaching a flat profile for asymptotic times.

Note that solution $v$ can be conveniently expressed in the form of a ring structure through the horizontal variables $X,Y$ at each time $T$, viz.,

$$v\left(X,Y,T\right)=\frac{1}{T}\left[u\left(\frac{\sqrt{X^2+Y^2}-T}{T^{1/2}},-\frac{2}{T^{1/2}}\right)+\frac{\sqrt{X^2+Y^2}-T}{3}\right]. \tag{14}$$

In the following, by means of such a construction, we find the analytical solutions of the ring-type multi-solitons for one-, two-, and three-soliton cases.

### A. One-soliton solutions

We express the solution of the concentric Eq. (7) as the image (by means of the above transformation) of the bright one-soliton solution of the pKdVE, given by $u(\xi,\tau)=u_{m0}\,\mathrm{sech}^2\left[\sqrt{3u_{m0}/4}\left(\xi-V_0\tau\right)\right]$, where $V_0=u_{m0}/2$. We may designate these concentric solutions as the *cylindrical (or concentric) bright one-soliton solution* with tilted boundary conditions, or simply *tilted* bright soliton. Therefore, a tilted one-soliton that is the solution

of Eq. (7) is given by [19, 20]

$$H_0(\zeta, s) = \frac{1}{s}\left\{\frac{\zeta}{3} + u_{m0}\,\mathrm{sech}^2\left[\sqrt{\frac{3\,u_{m0}}{4\,s}}\,(\zeta + u_{m0})\right]\right\}, \tag{15}$$

where $u_{m0}$ is the maximum amplitude of the corresponding planar soliton. Then, we rewrite the solution (15) in terms of the new variables $R$ and $T$, obtaining

$$v(R, T) = \frac{1}{T}\left\{\frac{1}{3}\,(R - T) + u_{m0}\,\mathrm{sech}^2\left[\sqrt{\frac{3\,u_{m0}}{4\,T}}\,[(R - T) + u_{m0}]\right]\right\}. \tag{16}$$

The spatiotemporal evolution in $(R, T)$ domain of tilted soliton (16) is displayed in Figure 1. The 3D plots displayed in Figure 2 show the spatiotemporal evolution of a tilted soliton, initially implemented ($T = T_{min}$) in the $(X, Y, T)$ domain. These plots represent the nonlinear water waves in the form of bright tilted ring solitons. We observe that, for $T > T_{min}$, the initial pulse profiles of the ring starts to propagate circularly. According to Eq. (16), as $T$ increases, both the amplitude of the soliton pulse and the slope of the oblique asymptote decrease; whilst, the width of the pulse increases. However, the pulse preserves its soliton shape during this evolution.

### B. Two- and three-soliton solutions

By applying the same transformation (8) to the two-and three-soliton solutions of pKdVE, we easily find also the analytical tilted solutions of Eq. (7) in the form of two- and three-tilted solitons, respectively.

#### *1. Two-soliton solution*

$$H_0(\zeta, s) = \frac{1}{s}\left[\frac{\zeta}{3} + (u_{m2} - u_{m1})\frac{P' + Q'}{S'^2}\right], \tag{17}$$

where

$$P' = u_{m1}\,\mathrm{sech}^2\left[\sqrt{\tfrac{3\,u_{m1}}{4\,s}}\,(\zeta + u_{m1})\right], \quad Q' = u_{m2}\,\mathrm{cosech}^2\left[\sqrt{\tfrac{3\,u_{m2}}{4\,s}}\,(\zeta + u_{m2})\right],$$
$$S' = \sqrt{u_{m1}}\tanh\left[\sqrt{\tfrac{3\,u_{m1}}{4\,s}}\,(\zeta + u_{m1})\right] - \sqrt{u_{m2}}\coth\left[\sqrt{\tfrac{3\,u_{m2}}{4\,s}}\,(\zeta + u_{m2})\right];$$

*2. Three-soliton solutions*

$$H_0(\zeta, s) = \frac{1}{s}\left[\frac{\zeta}{3} + P' - \frac{(u_{m2} - u_{m3})\, W'}{\left(\frac{u_{m1}-u_{m2}}{S'} - \frac{u_{m3}-u_{m1}}{T'}\right)^2}\right], \tag{18}$$

where

$$W' = \frac{(u_{m2}-u_{m1})(P'+Q')}{S'^2} + \frac{(u_{m3}-u_{m1})(R'-P')}{T'^2},\quad R' = u_{m3}\,\mathrm{sech}^2\left[\sqrt{\frac{3\,u_{m3}}{4\,s}}\,(\zeta + u_{m3})\right],$$
$$T' = \sqrt{u_{m3}}\tanh\left[\sqrt{\frac{3\,u_{m3}}{4\,s}}\,(\zeta + u_{m3})\right] - \sqrt{u_{m1}}\tanh\left[\sqrt{\frac{3\,u_{m1}}{4\,s}}(\zeta + u_{m1})\right].$$

Figures 3 and 4 [5 and 6] display the spatiotemporal evolution of an initially introduced two-tilted soliton [three-tilted soliton] solution ($T = T_{min}$), obtained by rewriting the analytical solution Eq. (17) [Eq. (18)] in the $(R, T)$ domain, according to Eq. (13), or in the $(X, Y, T)$ domain, according to Eq. (14).

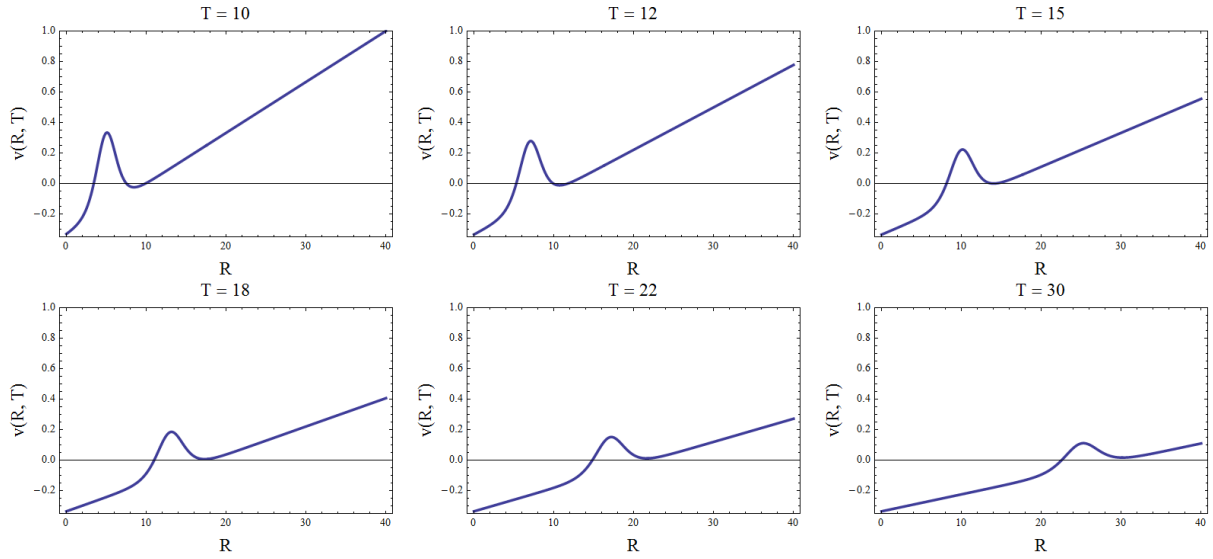


FIG. 1: Elevation $v$ of the analytical tilted one-soliton solution vs $R$ at fixed values of $T$. $u_{m0} = 5$ and $T_{min} = 10$.

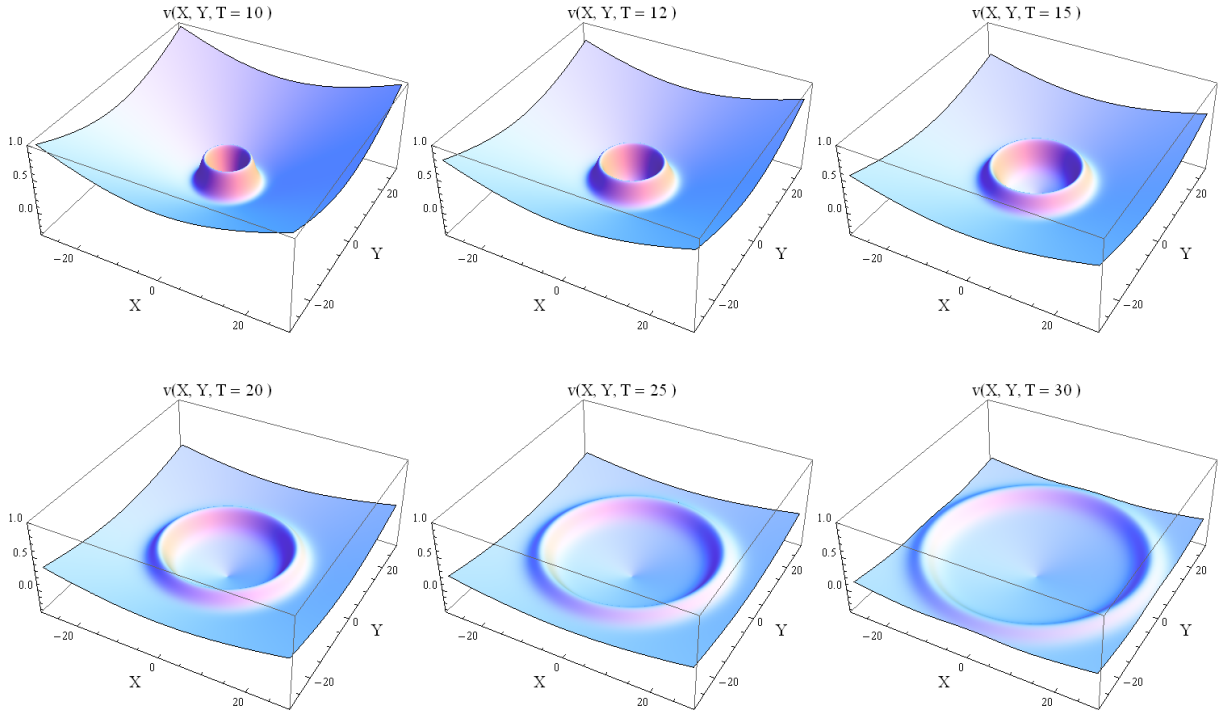


FIG. 2: Analytical spatial profile of the tilted ring-type one-soliton solution in $(X, Y, T)$ domain at fixed values of $T$. $u_{m0} = 5$ and $T_{min} = 10$.

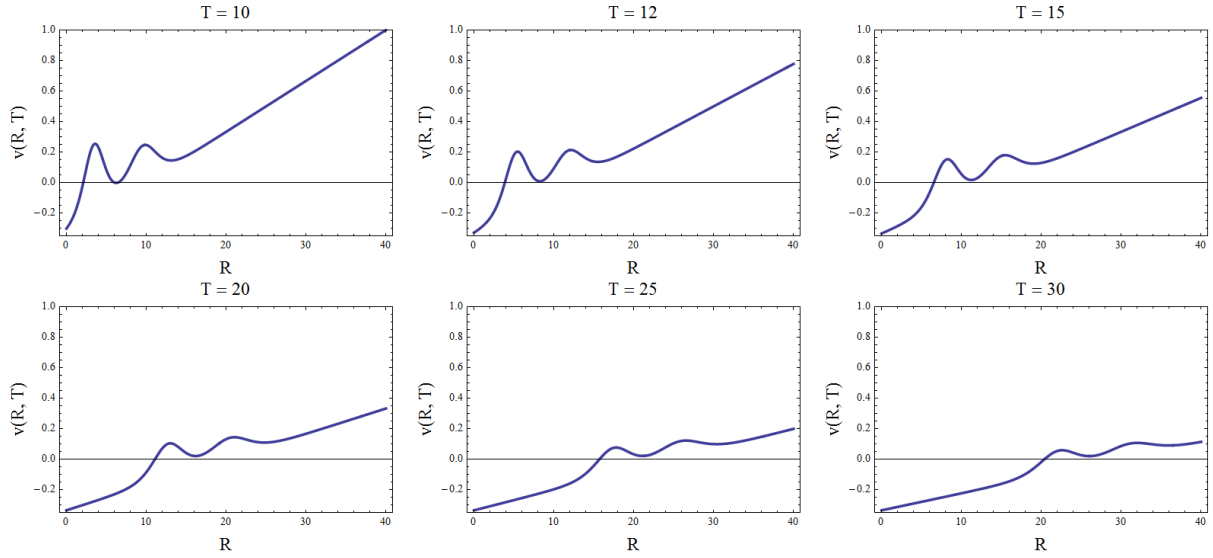


FIG. 3: Elevation $v$ of the analytical tilted two-soliton solution vs $R$ at fixed values of $T$. $u_{m1} = 2.5$, $u_{m2} = 5$, and $T_{min} = 10$.

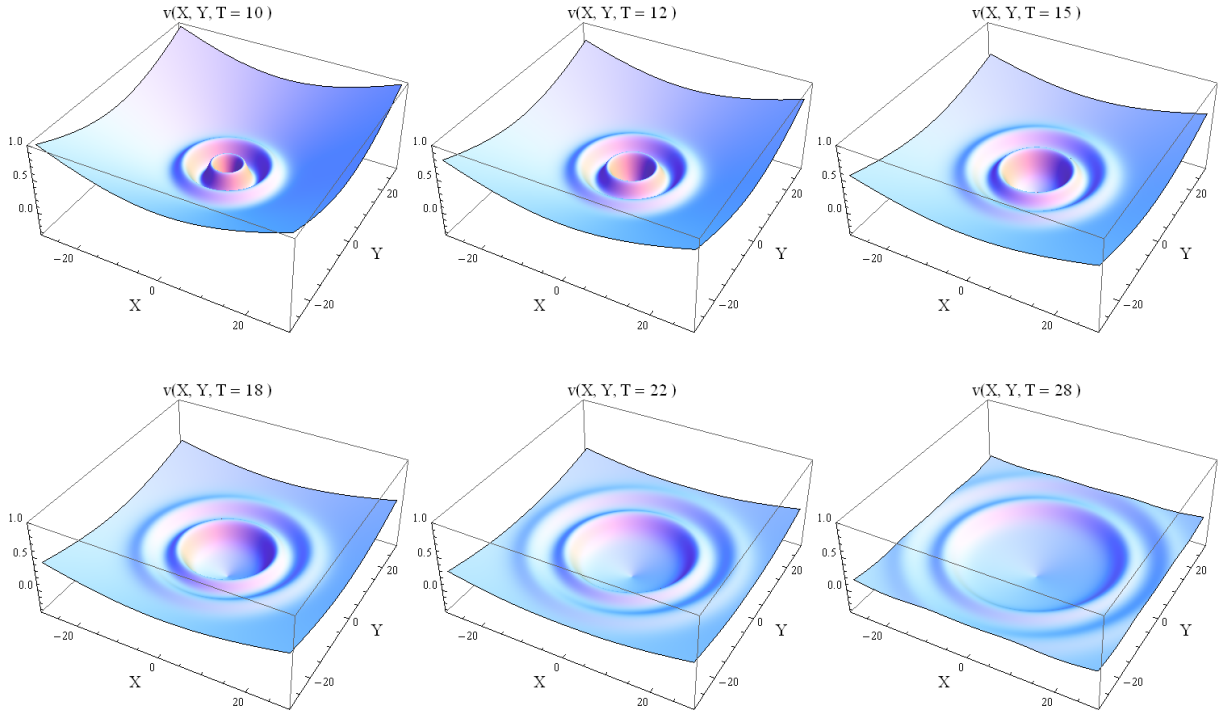


FIG. 4: Analytical tilted ring-type two-soliton solution in $(X, Y, T)$ domain at fixed values of $T$. $u_{m1} = 2.5$ and $u_{m2} = 5$, and $T_{min} = 10$.

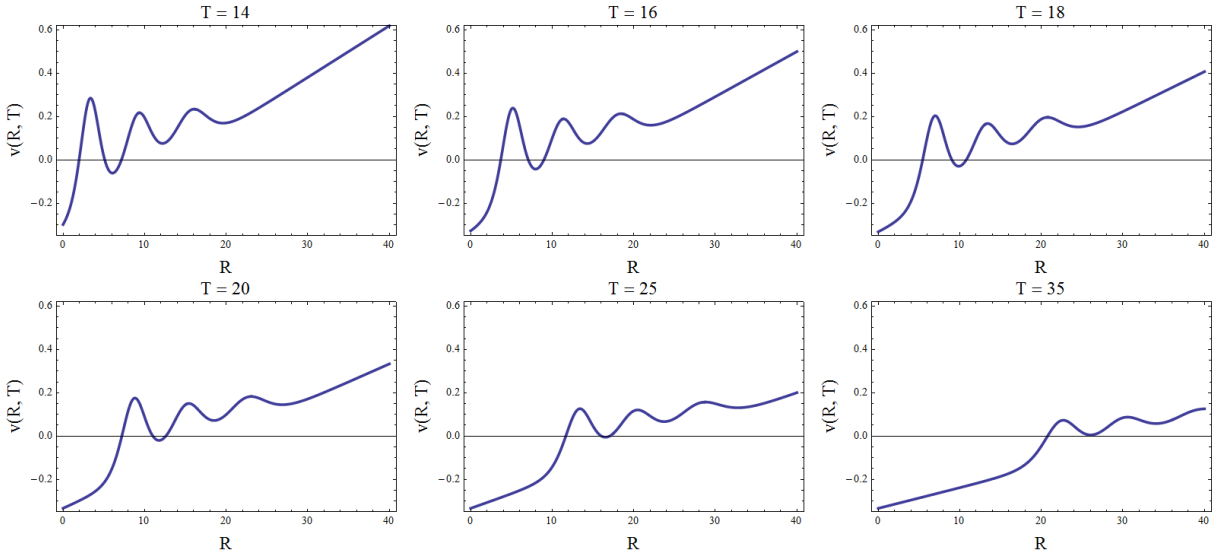


FIG. 5: Elevation $v$ of the analytical tilted three-soliton solution vs $R$ at fixed values of $T$. $u_{m1} = 2.5$, $u_{m2} = 5$, $u_{m3} = 8$, and $T_{min} = 14$.

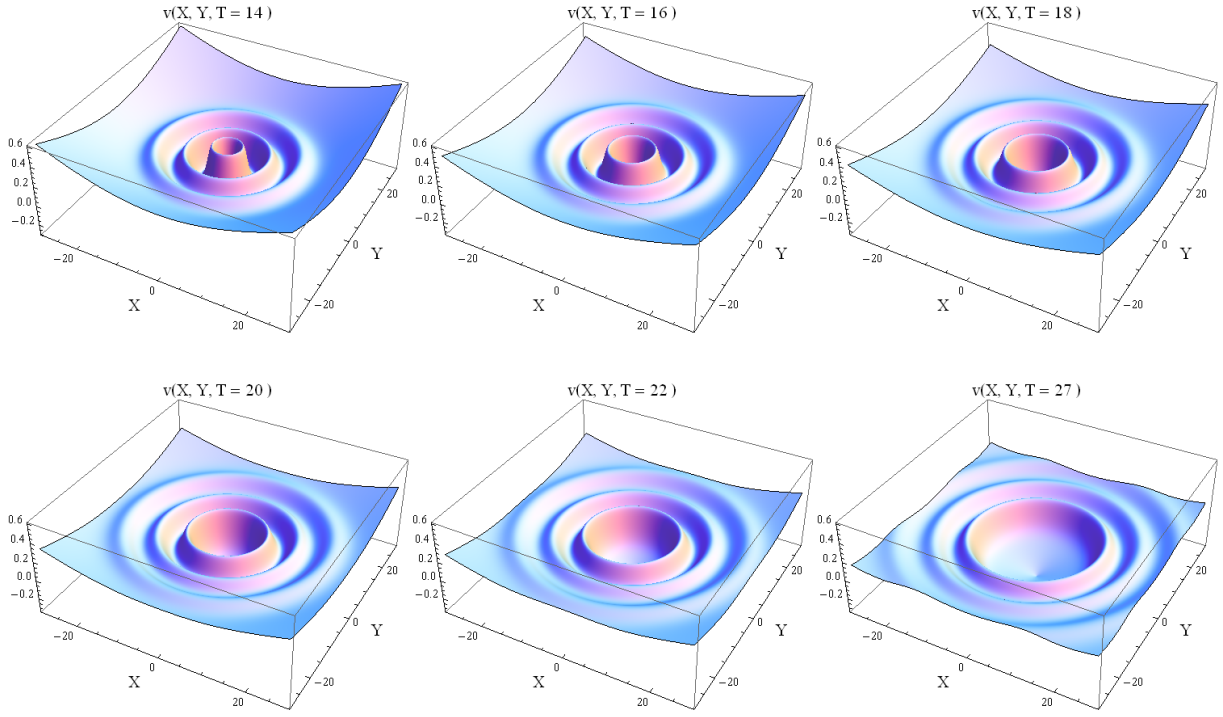


FIG. 6: Analytical tilted ring-type three-soliton solution in $(X, Y, T)$ domain. $u_{m1} = 2.5$, $u_{m2} = 5$, and $u_{m3} = 8$, and $T_{min} = 14$.

## IV. OVERVIEW OF THE RESULTS CONCERNING THE ANALYTICAL TILTED RING SOLITONS

The attentive analysis of the results presented in section III has allowed us to note certain features that are summarized and discussed below.

All our analytical results on the spatiotemporal evolution of the water wave elevation, see Figures 1 – 6, deal with multi-ring profiles in the form of one-, two- or three-ring soliton pulses. For arbitrary times $T$, $T > T_{min}$, these initial structures evolve as the result of their free fall and is governed by Eq. (10). Our analysis is performed by comparing the features of a tilted soliton, observed in the previous section, with those typically ascribed to a soliton-like behaviour in the planar case.

### A. General physiognomy of the analytical localized tilted structures during the spatiotemporal evolution

First of all, we observe that the localized solutions found in this work appear as: (a) single- or multi-pulse structures that are propagating to the right, in $(R, T)$ domain; (b) single- or multi-ring structures propagating outward (divergent rings), in $(X, Y, T)$ domain. According to Figures 1, 3 and 5, each tilted multi-soliton can be thought, in $(R, T)$ domain, as the superposition of a flat, oblique profile, which determines their tilted asymptotic behavior, and a multi-soliton with standard boundary conditions, whose peak amplitude decreases as $T$ increases. As $T$ increases, a clockwise rotation of the asymptote toward the $R$ axis takes place. According to Figures 2, 4 and 6, the corresponding tilted ring-type multi-solitons can be thought as the superposition of a conic-shaped water surface and a standard ring-type multi-solitons.

### B. Physiological temporal decay of the amplitudes

As we will see also in next sections for the numerical solutions, cylindrical solitons are affected by a temporal decay of their amplitudes. This is an intrinsic effect related to the geometrical character of these solutions. We refer it to as the *physiological decay* of the cylindrical solitons. Figures 1 – 6 show the physiological decay for tilted bright multi-ring solitons. Solutions (16), (17) and (18) show that each ring (or pulse) amplitude decays as $1/T$.

### C. Complementarity between amplitude and width in a single-pulse

The soliton physiological decay is always accompanied by the temporal growth of the pulse width. We refer it to as the *physiological spreading* of the cylindrical solitons. It is clearly visible in Figures 1 – 6 through their spreading. Physiological decay and physiological spreading (flattening) are always complementary effects. According to solutions (16), (17) and (18), the pulse width growths as $\sqrt{T}$. Remarkably, we note that, on the basis of these two temporal laws, the *amplitude-width* complementarity is ruled by the following law: $u_m(T)\,\sigma(T)^2 =$ constant, where $u_m(T)$ and $\sigma(T)$ are, at any time, the instantaneous amplitude and width of the soliton, respectively. Since, for very large $T$, Eq. (7) reduces

to the pKdVE, this law asymptotically recovers the well-known constancy of the product $u_m\,\sigma^2$ (determined by the coefficients of the pKdVE) that holds for planar solitons.

### D. Physiological temporal tilting reduction

Another *physiological* effects exhibited by the analytical solutions (16), (17) and (18) is the temporal *reduction of the tilt*. According to Figures 1, 3 and 5, as $T$ increases, a clockwise rotation of the asymptote toward the $R$ axis takes place. Therefore, for asymptotic times, the tilted boundary conditions corresponding to the above solutions tend to reduce to the standard ones. Note that the soliton-like shape of each pulse/ring is unaffected by the tilt during the temporal evolution.

### E. Dependence of ring velocity on ring amplitude

According to Eqs. (15) - (18), all the soliton-like pulses/rings of the tilted multi-solitons are standing, in the $(\zeta, s)$ domain, or move along $R$ to the right with the same speed, in the $(R, T)$ domain. We have never observed, in any of our two- and three-soliton solutions, that a higher pulse overcomes a smaller one, as it typically occurs in the case of the pKdV solitons. Such a behavior actually confirms that all the pulses/rings of the tilted multi-soliton structures have the same speed. We conclude that, for the cases investigated in this section, the velocity of each soliton pulse/ring is independent of its amplitude. In fact, one of the peculiarities of the transformation (13) or (14) is to transform multi-soliton solutions of the pKdVE (where each soliton pulse evolves with its own speed) into multi-pulse/multi-ring structures in which all the pulses/rings have the same speed (this way, the overcoming of a pulse by another one is forbidden for tilted solutions).

### F. Other features

During the evolution of analytical tilted soliton solutions, we have never observed the break-up of a tilted localized structure (either a single- or a multi-soliton) into two or more pulses. In addition, no enhancement of pulses has been ever observed, either. But, nevertheless, each pulse obeys to the amplitude-width complementarity law, i.e., although maximum

amplitude and width of each pulse experience the physiological variation, the instantaneous product $(maximum\ amplitude) \times (width)^2$ is rigorously constant. This law, typically ascribed to a soliton-like behaviour, is satisfied while each pulse/ring preserves rigorously at each time the soliton shape

## V. NUMERICAL SOLUTIONS: RING-TYPE SOLITONS WITH STANDARD BOUNDARY CONDITIONS

In this section, we are going to solve numerically Eq. (10), i.e., to find numerically the spatiotemporal evolution of an initially imposed multi-soliton profile at $T = T_{min} > 0$, with standard boundary conditions in $(R, T)$ domain. Then, according to the results of section II B, we express $v$ in the $(X, Y, T)$ domain in the form of a ring-type multi-soliton.

### A. Single-soliton solutions

Equation (10) has been solved using the initial conditions $(T = T_{min})$ i.e.,

$$v\,(R, T_{min}) = R^n\, u_{m0}\, \mathrm{sech}^2 \left[ \sqrt{\frac{3\, u_{m0}}{4}}\ (R - R_0) \right], \quad n = 0, 4\,, \tag{19}$$

where $R_0$ is an arbitrary positive constant for $n = 0, 4$. As we have used a finite-sized computational box, the standard boundary conditions

$$\lim_{R\to 0} v\,(R, T) \;=\; \lim_{R\to\infty} v\,(R, T)\ .$$

has been substituted by the appropriate periodic boundary condition, viz.

$$v(R = 0, T) = v(R = R_{max}, T) \tag{20}$$

for $R_{max}$ sufficiently large. In Figures 7 and 9 we show the spatiotemporal evolution of the numerical solutions of Eq. (10) that correspond to the initial conditions (19), with $n = 0$ and $R_0 = 10$, and boundary conditions (20). Here we have used the initial condition at two different values of $T_{min}$: $T_{min} = 5$ (Figure 7) and $T_{min} = 1$ (Figure 9). We can see that the height of the soliton decreases as the function of $T$, when $T_{min} = 5$, more slowly than in the case $T_{min} = 1$. With the same initial and boundary conditions, but taking $n = 4$ and $R_0 = 0$, we have found the numerical solutions that are displayed in Figures 11 and 13. All

the above numerical solutions, once expressed in $(X, Y, T)$ domain (i.e., $R = \sqrt{X^2 + Y^2}$), give the ring-type water waves solitons whose spatiotemporal evolution is shown in Figures 8, 10, 12, and 14. In Figures 15 and 16, the solution of Eq. (10) is displayed in the $(R, T)$ domain in the case of $R_0 \neq 0$ and $n = 4$.

### B. Two- and three-soliton solutions

Further numerical localized solutions of Eq. (10) have been found with the boundary conditions (20) and the following two- and three- soliton-like initial conditions, respectively, i.e.,

$$v(R, T_{min}) = (u_{m2} - u_{m1}) \frac{P + Q}{S^2}\,, \tag{21}$$

where

$$P = u_{m1}\,\mathrm{sech}^2\left[\sqrt{\tfrac{3\,u_{m1}}{4}}\,(R - R_1)\right], \quad Q = u_{m2}\,\mathrm{cosech}^2\left[\sqrt{\tfrac{3\,u_{m2}}{4}}\,(R - R_2)\right],$$
$$S = \sqrt{u_{m1}}\tanh\left[\sqrt{\tfrac{3\,u_{m1}}{4}}(R - R_1)\right] - \sqrt{u_{m2}}\coth\left[\sqrt{\tfrac{3\,u_{m2}}{4}}(R - R_2)\right],$$

and

$$v(R, T_{min}) = P - \frac{u_{m2} - u_{m3}}{\left(\frac{u_{m1} - u_{m2}}{S} - \frac{u_{m3} - u_{m1}}{L}\right)^2}\left[\frac{(u_{m2} - u_{m1})(P + Q)}{S^2} + \frac{(u_{m3} - u_{m1})(F - P)}{L^2}\right], \tag{22}$$

where

$$F = u_{m3}\,\mathrm{sech}^2\left[\sqrt{\tfrac{3\,u_{m3}}{4}}(R - R_3)\right],$$
$$L = \sqrt{u_{m3}}\tanh\left[\sqrt{\tfrac{3\,u_{m3}}{4}}(R - R_3)\right] - \sqrt{u_{m1}}\tanh\left[\sqrt{\tfrac{3\,u_{m1}}{4}}(R - R_1)\right].$$

In the equations above, $u_{m1}$, $u_{m2}$, $u_{m3}$, $R_1$, $R_2$ and $R_3$ are positive arbitrary constants. Figures 17 – 20 [Figures 21 – 24] exhibit the spatiotemporal evolution of the above initially given two-solitonlike profile (21) [three-solitonlike profile (22)] in $(R, T)$ and $(X, Y, T)$ domains, respectively. We have also studied numerically two- and three-soliton profiles with the same boundary conditions and different initial conditions, viz.,

$$v\,(R, T_{min}) = R^n\,P + u_{m2}\,\mathrm{sech}^2\left[\sqrt{\frac{3\,u_{m2}}{4}}\,(R - R_2)\right] \tag{23}$$

and

$$v\,(R, T_{min}) = R^n\,P + u_{m2}\,\mathrm{sech}^2\left[\sqrt{\frac{3\,u_{m2}}{4}}\,(R - R_2)\right] + F\,. \tag{24}$$

Figure 25 [Figure 27] shows the two soliton [three soliton] solution as function of $R$ at fixed values of $T$. In addition, Figure 26 [Figure 28] displays the numerical ring-type two-soliton [three-soliton] solutions in $(X, Y, T)$ domain at the fixed values of $T$.

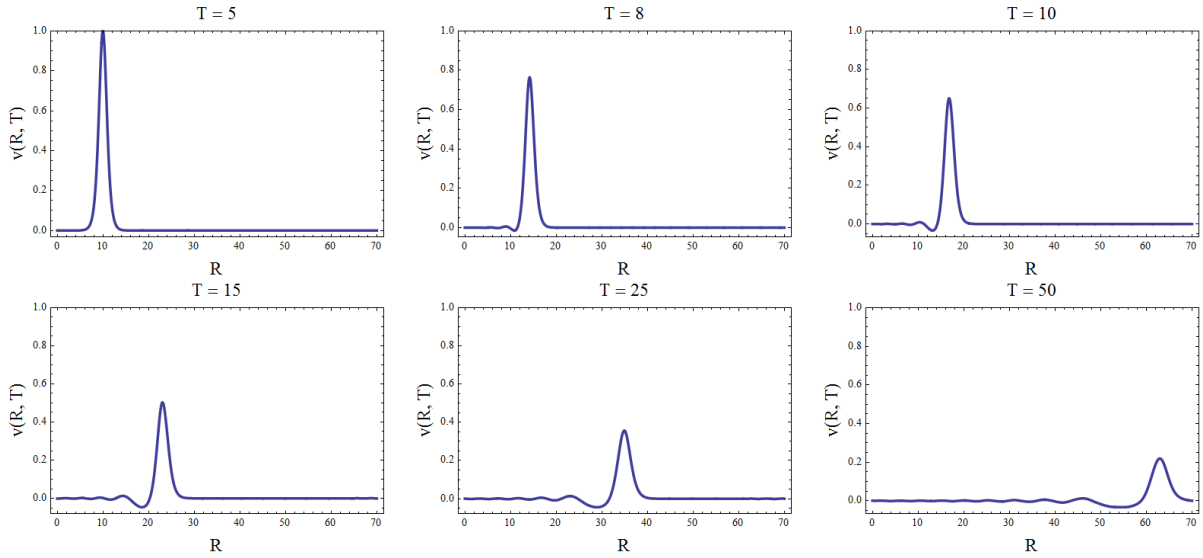


FIG. 7: Elevation $v$ of the numerical solution of cKdVE, i.e., Eq. (10), vs $R$ at fixed values of $T$, satisfying the boundary condition (20). The initial condition is fixed according to Eq. (19), where $n = 0$, $R_0 = 10$, $u_{m0} = 1$, and $T_{min} = 5$.

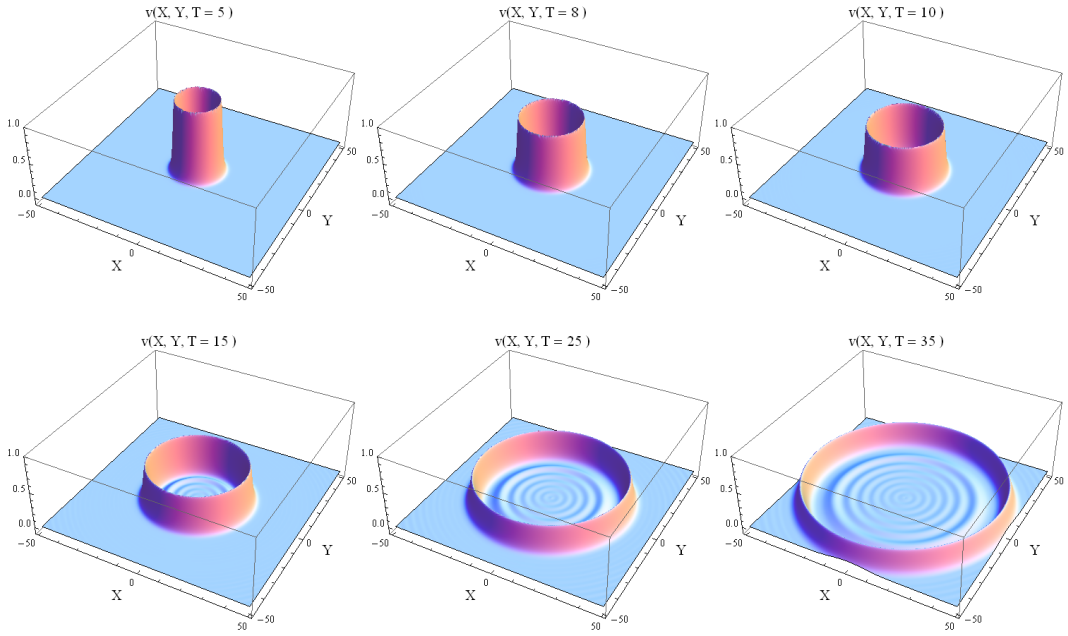


FIG. 8: Numerical ring-type solution of cKdVE, i.e., Eq. (10) in $(X, Y, T)$ domain. The initial condition is fixed according to Eq. (19), where $n = 0$, $R_0 = 10$, $u_{m0} = 1$, and $T_{min} = 5$.

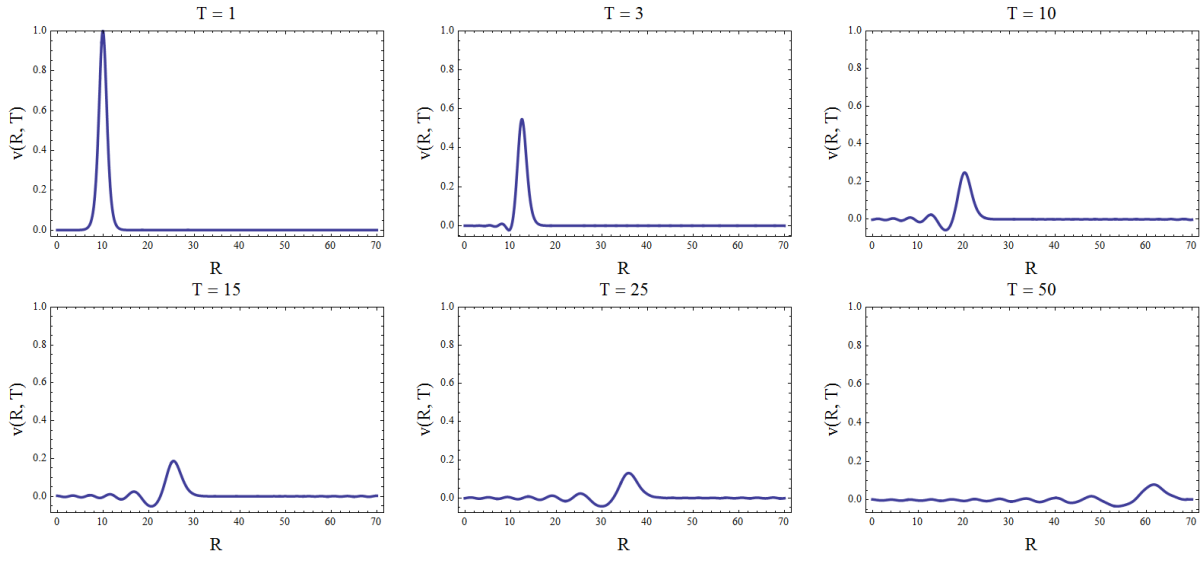


FIG. 9: Elevation $v$ of the numerical solution of cKdVE, i.e., Eq. (10), vs $R$ at fixed values of $T$, satisfying the boundary condition (20). The initial condition is fixed according to Eq. (19), where $n = 0$, $R_0 = 10$, $u_{m0} = 1$, and $T_{min} = 1$.

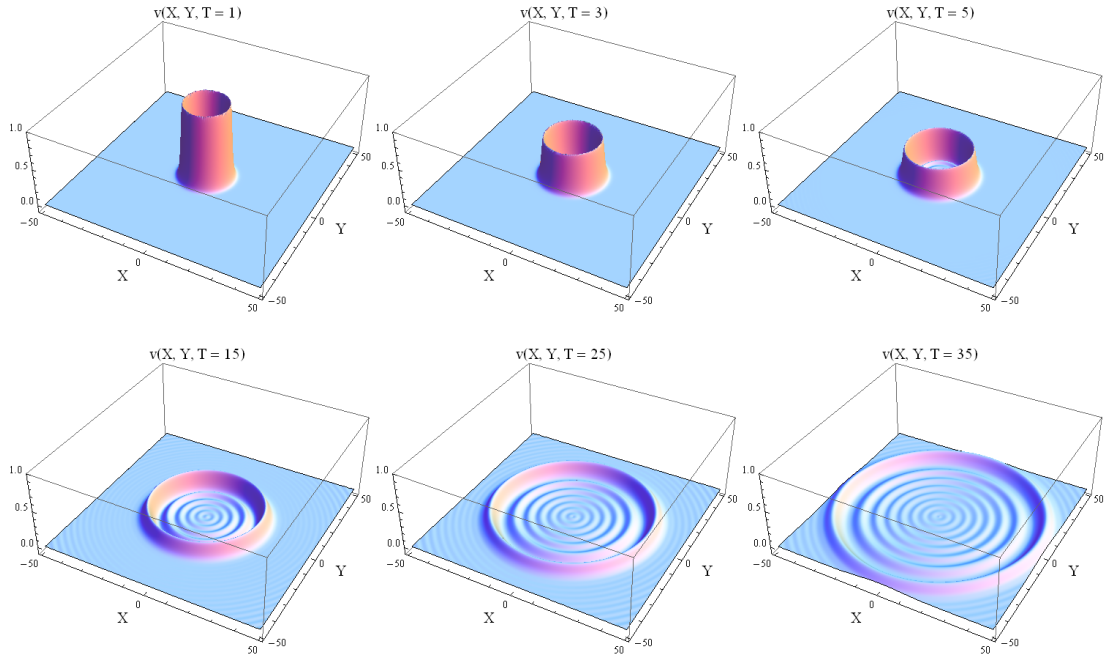


FIG. 10: Numerical ring-type solution of cKdVE, i.e., Eq. (10) in $(X, Y, T)$ domain. The initial condition is fixed according to Eq. (19), where $n = 0$, $R_0 = 10$, $u_{m0} = 1$, and $T_{min} = 1$.

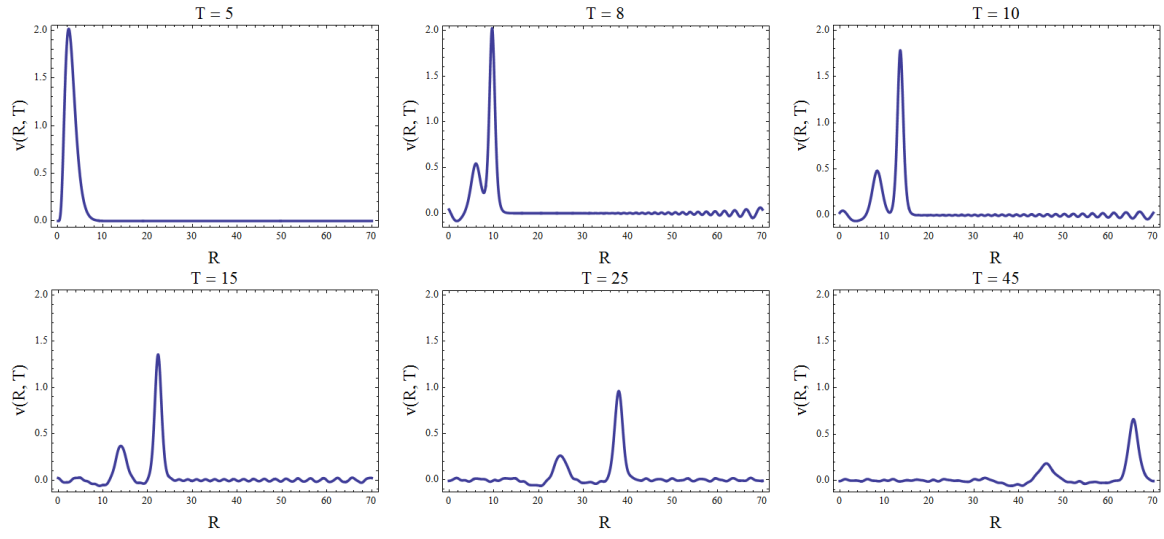


FIG. 11: Elevation $v$ of the numerical solution of cKdVE, i.e., Eq. (10), vs $R$ at fixed values of $T$, satisfying the boundary condition (20). The initial condition is fixed according to Eq. (19), where $n = 4$, $R_0 = 0$, $u_{m0} = 1$, and $T_{min} = 5$.

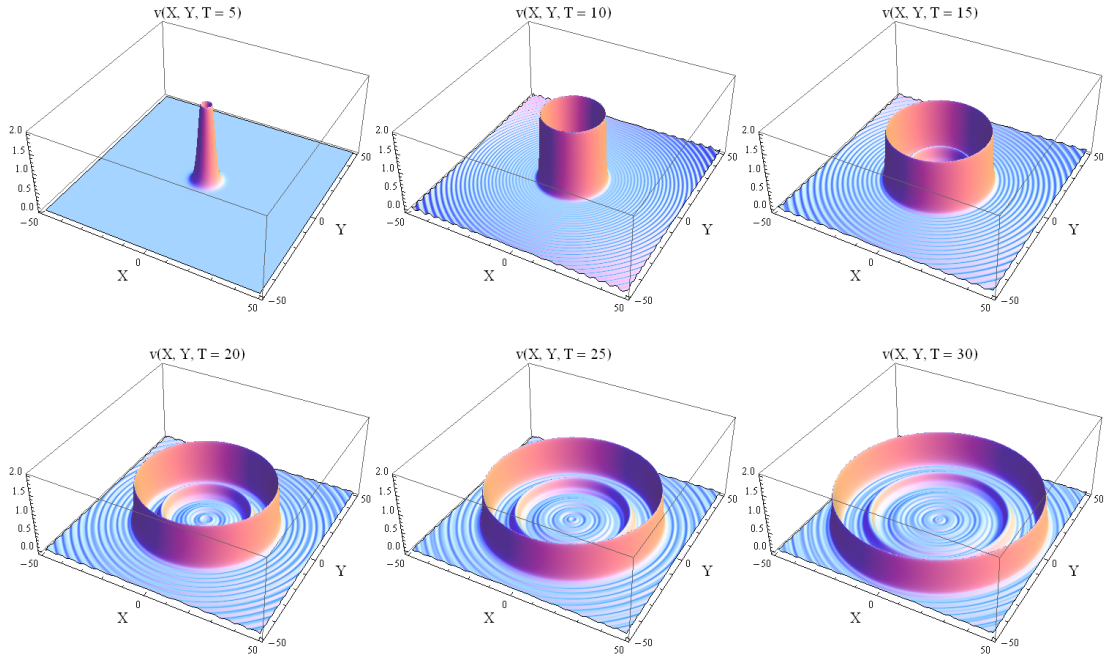


FIG. 12: Numerical ring-type solution of cKdVE, i.e., Eq. (10) in $(X, Y, T)$ domain. The initial condition is fixed according to Eq. (19), where $n = 4$, $R_0 = 0$, $u_{m0} = 1$, and $T_{min} = 5$.

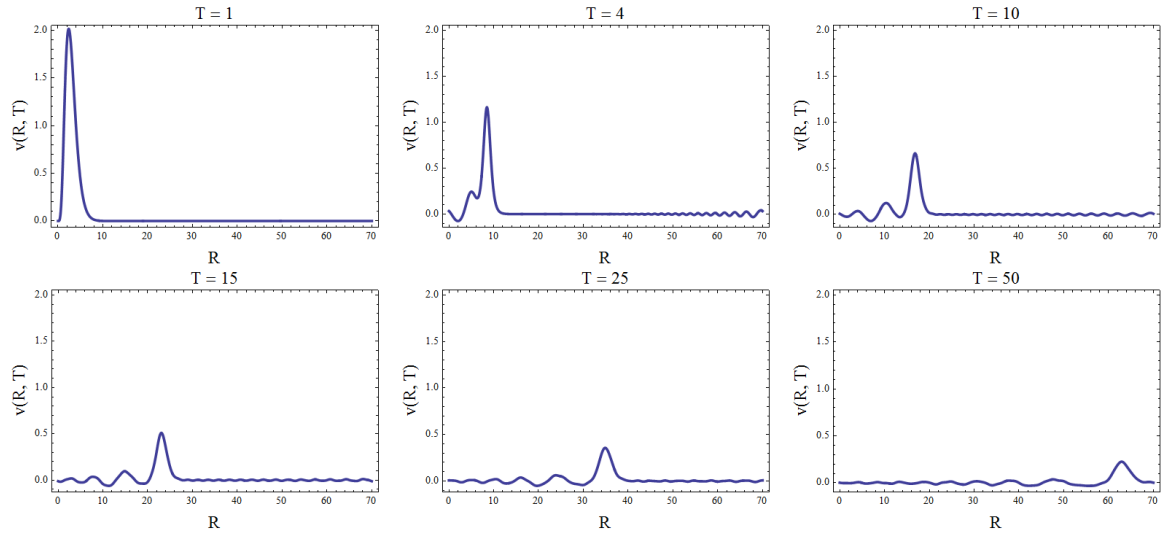


FIG. 13: Elevation $v$ of the numerical solution of cKdVE, i.e., Eq. (10), vs $R$ at fixed values of $T$, satisfying the boundary condition (20). The initial condition is fixed according to Eq. (19), where $n = 4$, $R_0 = 0$, $u_{m0} = 1$, and $T_{min} = 1$.

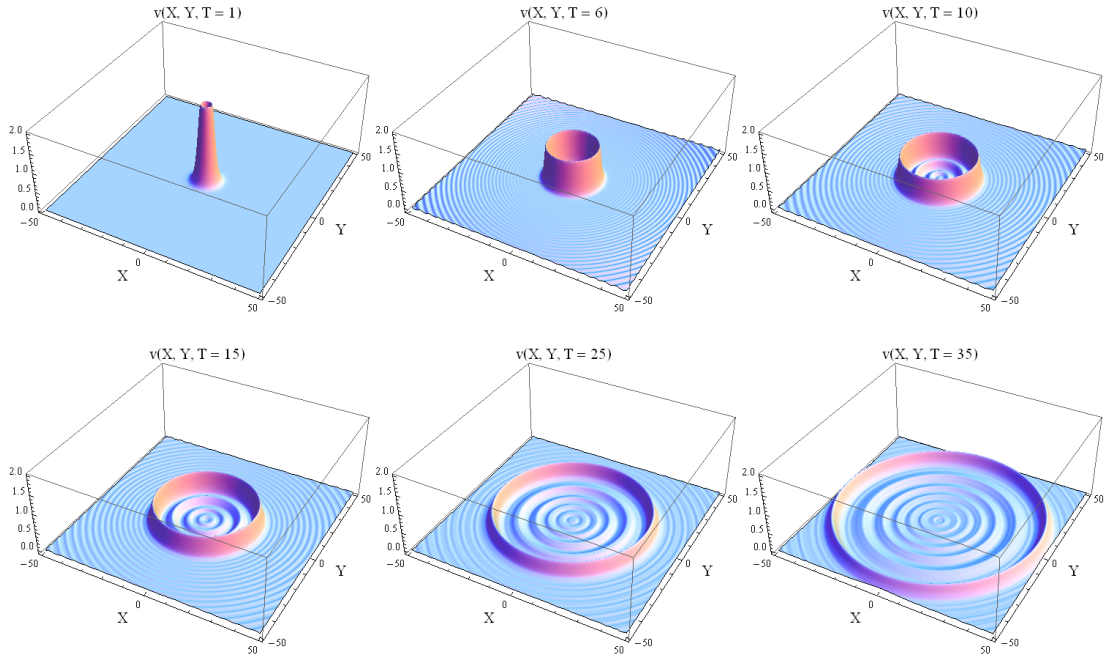


FIG. 14: Numerical ring-type solution of cKdVE, i.e., Eq. (10) in $(X, Y, T)$ domain. The initial condition is fixed according to Eq. (19), where $n = 4$, $R_0 = 0$, $u_{m0} = 1$, and $T_{min} = 1$.

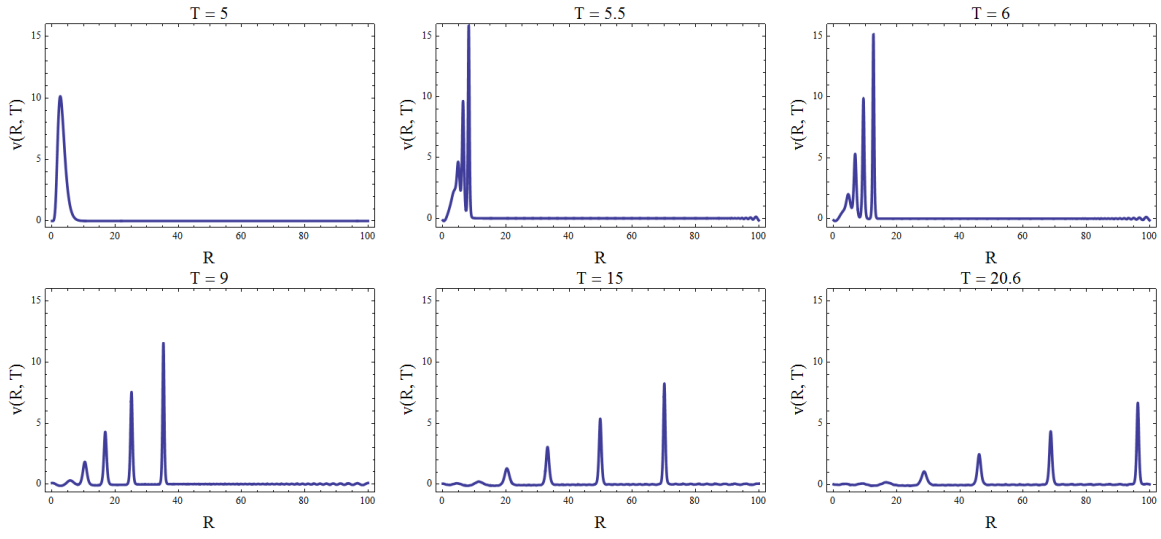


FIG. 15: Elevation $v$ of the numerical solution of cKdVE, i.e., Eq. (10), vs $R$ at fixed values of $T$, satisfying the boundary condition (20). The initial condition is fixed according to Eq. (19), where $n = 4$, $R_0 = 1$, $u_{m0} = 1$, and $T_{min} = 5$.

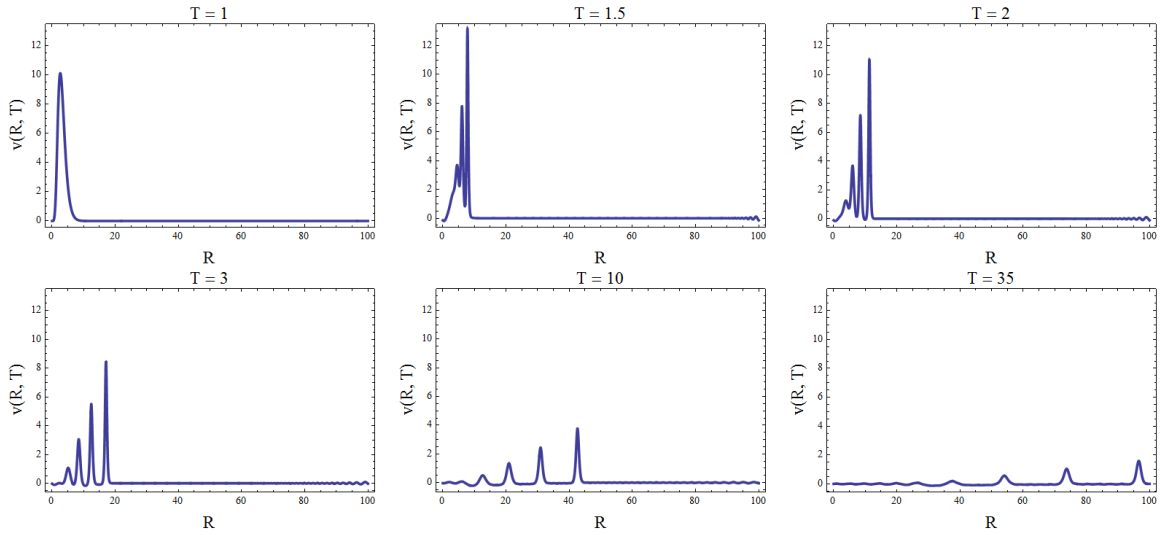


FIG. 16: Elevation $v$ of the numerical solution of cKdVE, i.e., Eq. (10), vs $R$ at fixed values of $T$, satisfying the boundary condition (20). The initial condition is fixed according to Eq. (19), where $n = 4$, $R_0 = 1$, $u_{m0} = 1$, and $T_{min} = 1$.

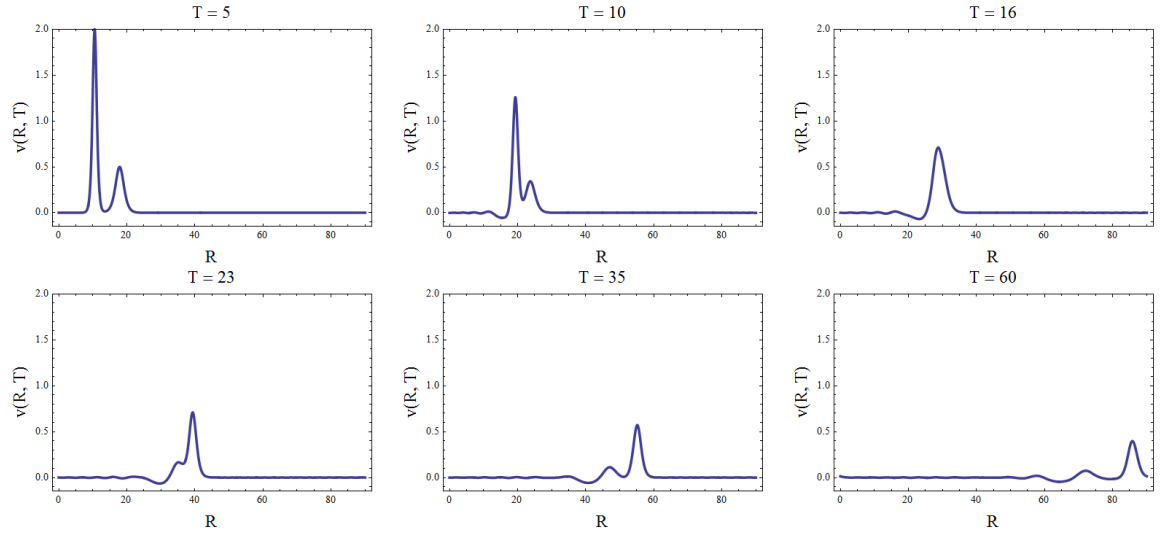


FIG. 17: Elevation $v$ of the numerical solution of cKdVE, i.e., Eq. (10), vs $R$ at fixed values of $T$, satisfying the boundary condition (20). The initial condition is fixed according to Eq. (21), where $u_{m1} = 0.5$, $u_{m2} = 2$, $R_1 = 17$, $R_2 = 11$, and $T_{min} = 5$.

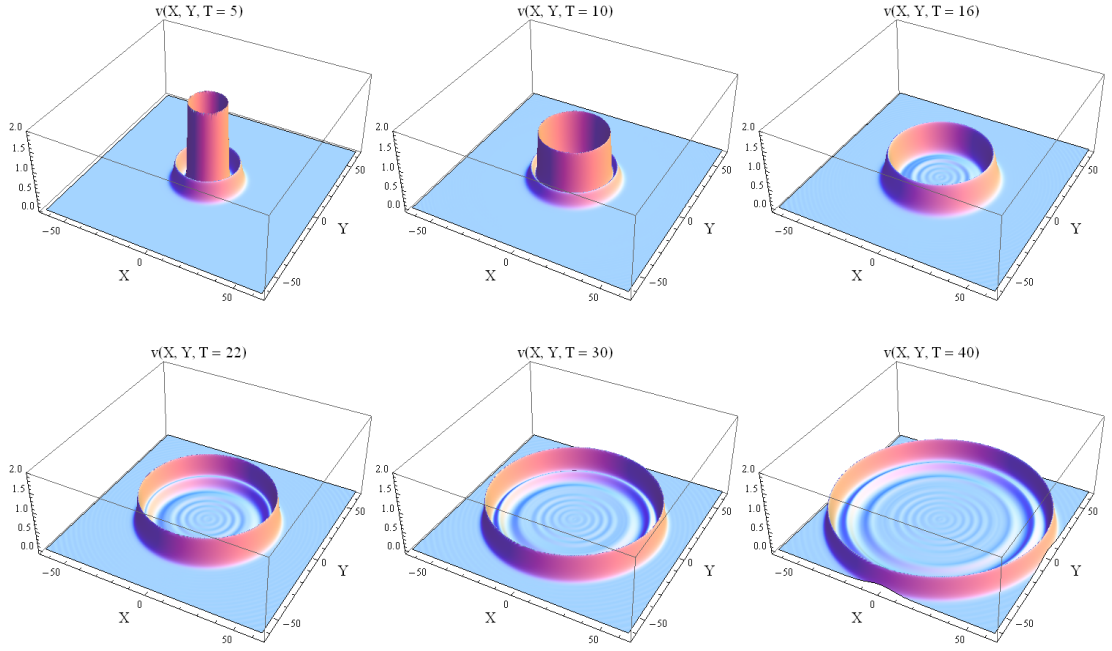


FIG. 18: Numerical ring-type solution of cKdVE, i.e., Eq. (10) in $(X, Y, T)$ domain. The initial condition is fixed according to Eq. (21), where $u_{m1} = 0.5$, $u_{m2} = 2$, $R_1 = 17$, $R_2 = 11$, and $T_{min} = 5$.

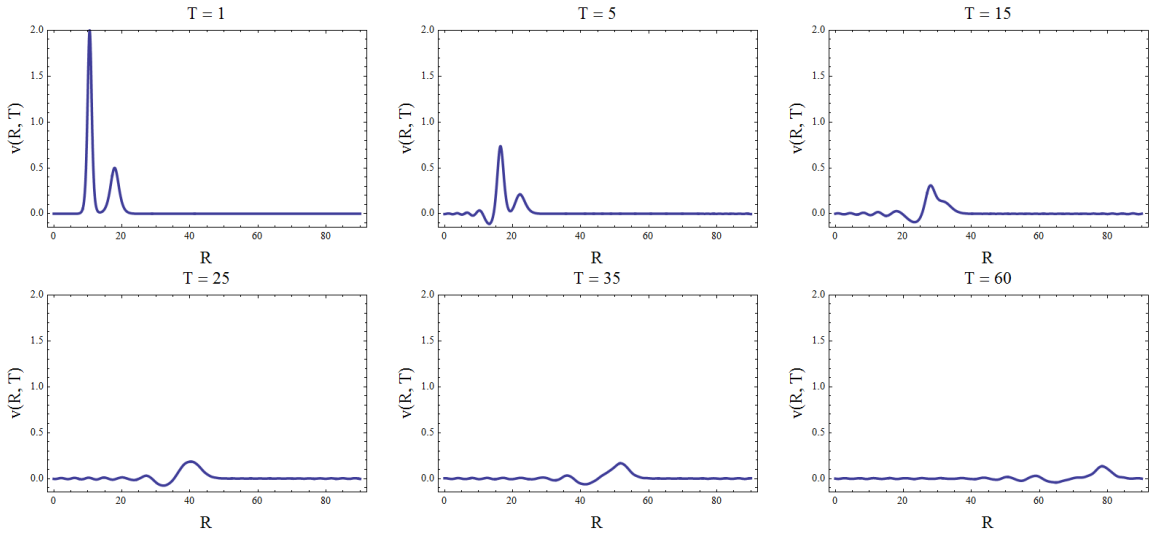


FIG. 19: Elevation $v$ of the numerical solution of cKdVE, i.e., Eq. (10), vs $R$ at fixed values of $T$, satisfying the boundary condition (20). The initial condition is fixed according to Eq. (21), where $u_{m1} = 0.5$, $u_{m2} = 2$, $R_1 = 17$, $R_2 = 11$, and $T_{min} = 1$.

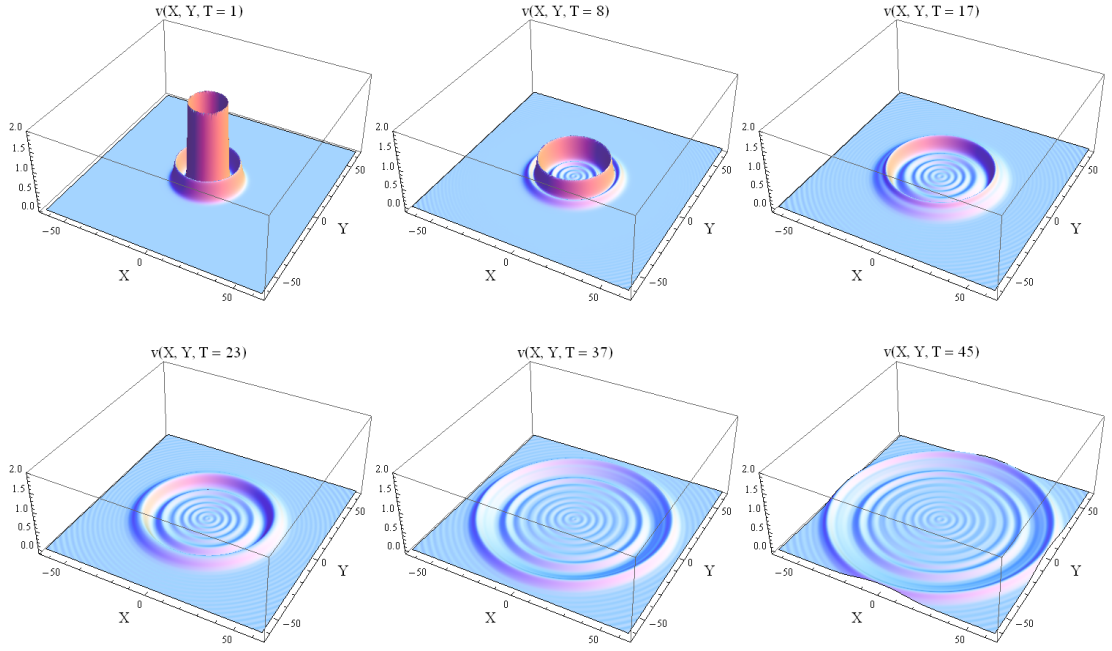


FIG. 20: Numerical ring-type solution of cKdVE, i.e., Eq. (10) in $(X, Y, T)$ domain. The initial condition is fixed according to Eq. (21), where $u_{m1} = 0.5$, $u_{m2} = 2$, $R_1 = 17$, $R_2 = 11$, and $T_{min} = 1$.

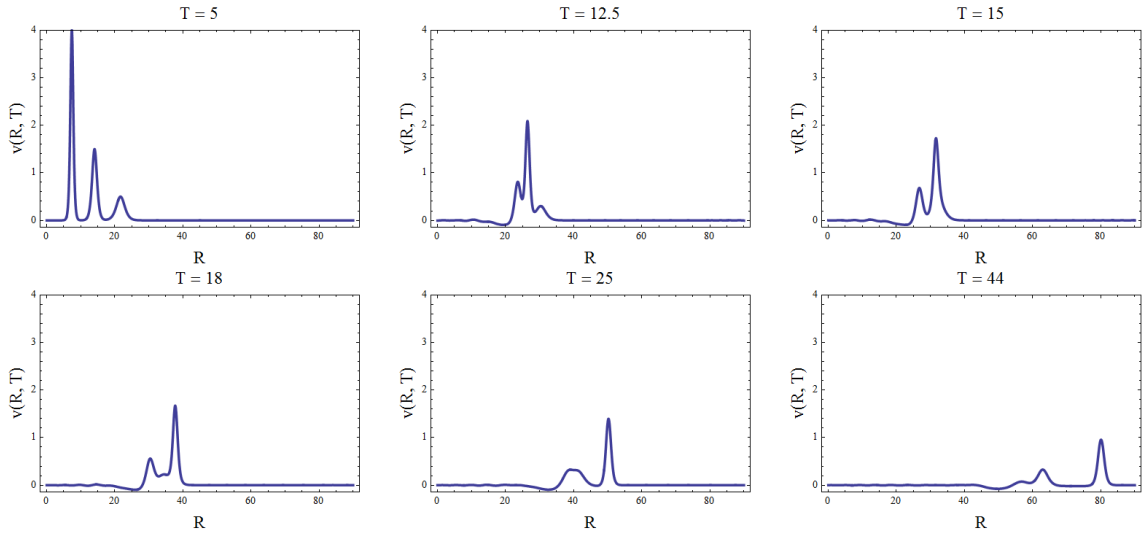


FIG. 21: Elevation $v$ of the numerical solution of cKdVE, i.e., Eq. (10), vs $R$ at fixed values of $T$, satisfying the boundary condition (20). The initial condition is fixed according to Eq. (22), where $u_{m1} = 0.5$, $u_{m2} = 1.5$, $u_{m3} = 4$, $R_1 = 20$, $R_2 = 14$, $R_3 = 8$, and $T_{min} = 5$.

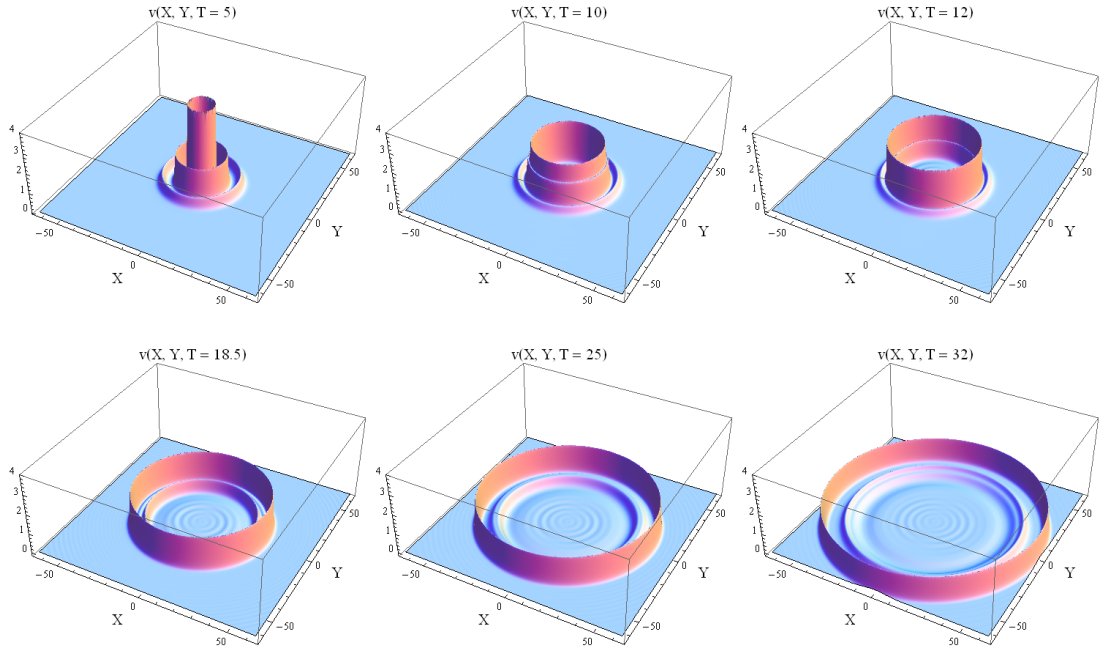


FIG. 22: Numerical ring-type solution of cKdVE, i.e., Eq. (10) in $(X, Y, T)$ domain. The initial condition is fixed according to Eq. (22), where $u_{m1} = 0.5$, $u_{m2} = 1.5$, $u_{m3} = 4$, $R_1 = 20$, $R_2 = 14$, $R_3 = 8$, and $T_{min} = 5$.

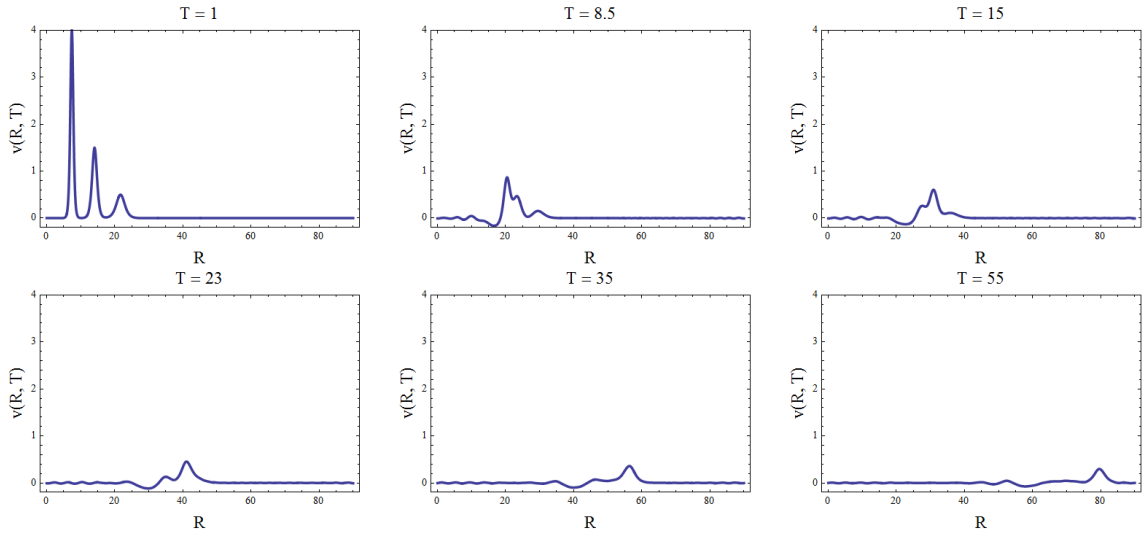


FIG. 23: Elevation $v$ of the numerical solution of cKdVE, i.e., Eq. (10), vs $R$ at fixed values of $T$, satisfying the boundary condition (20). The initial condition is fixed according to Eq. (22), where $u_{m1} = 0.5$, $u_{m2} = 1.5$, $u_{m3} = 4$, $R_1 = 20$, $R_2 = 14$, $R_3 = 8$, and $T_{min} = 1$.

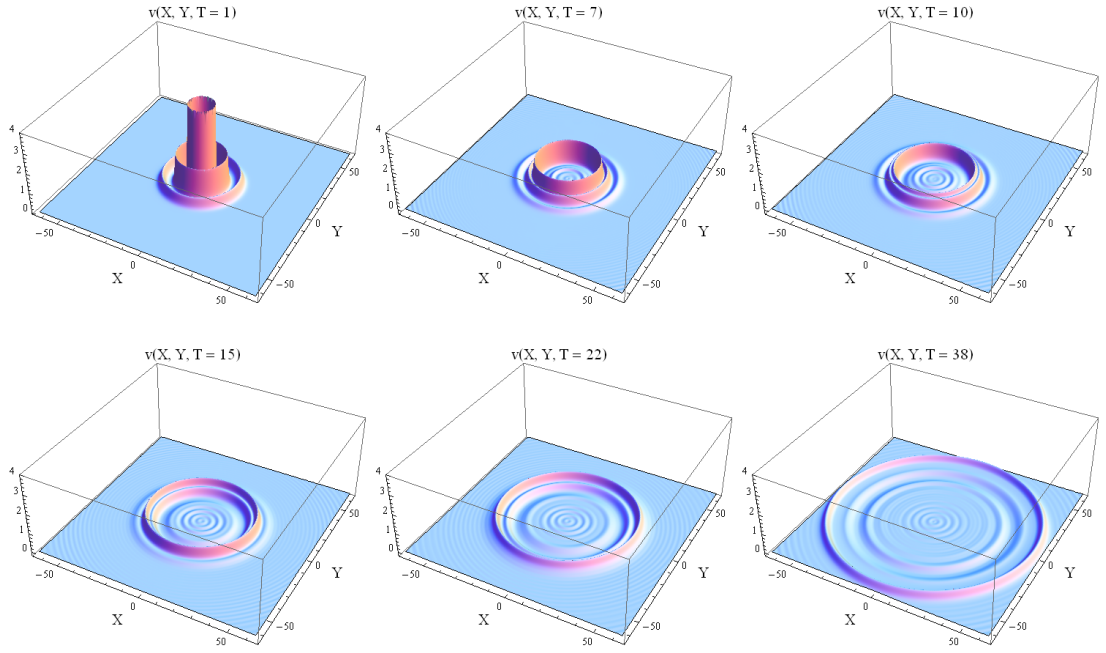


FIG. 24: Numerical ring-type solution of cKdVE, i.e., Eq. (10) in $(X, Y, T)$ domain. The initial condition is fixed according to Eq. (22), where $u_{m1} = 0.5$, $u_{m2} = 1.5$, $u_{m3} = 4$, $R_1 = 20$, $R_2 = 14$, $R_3 = 8$, and $T_{min} = 1$.

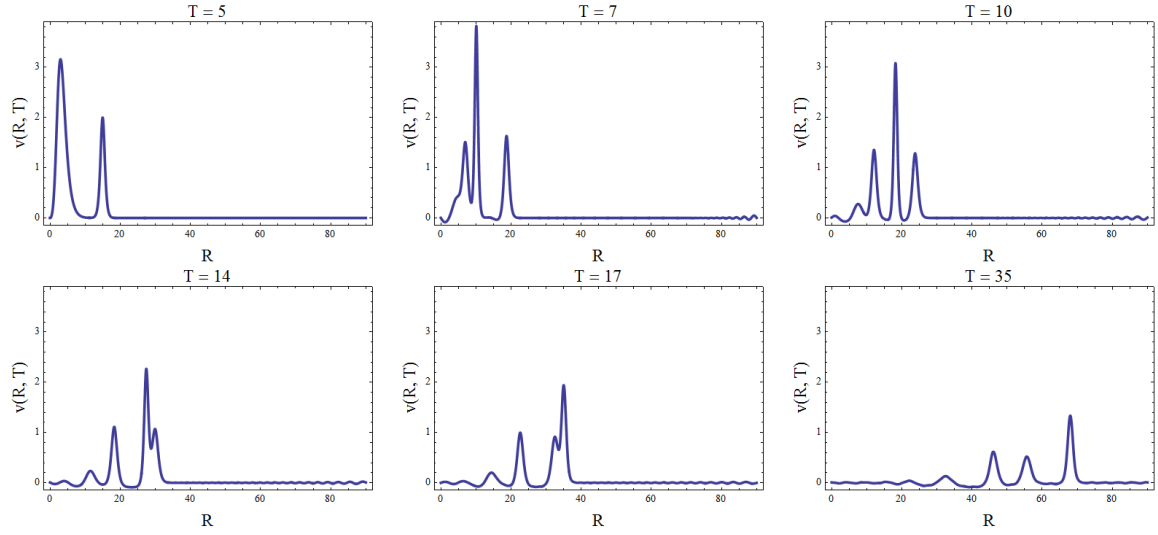


FIG. 25: Elevation $v$ of the numerical solution of cKdVE, i.e., Eq. (10), vs $R$ at fixed values of $T$, satisfying the boundary condition (20). The initial condition is fixed according to Eq. (23), where $n = 2$, $u_{m1} = 0.5$, $u_{m2} = 2$, $R_1 = 2$, $R_2 = 15$, and $T_{min} = 5$.

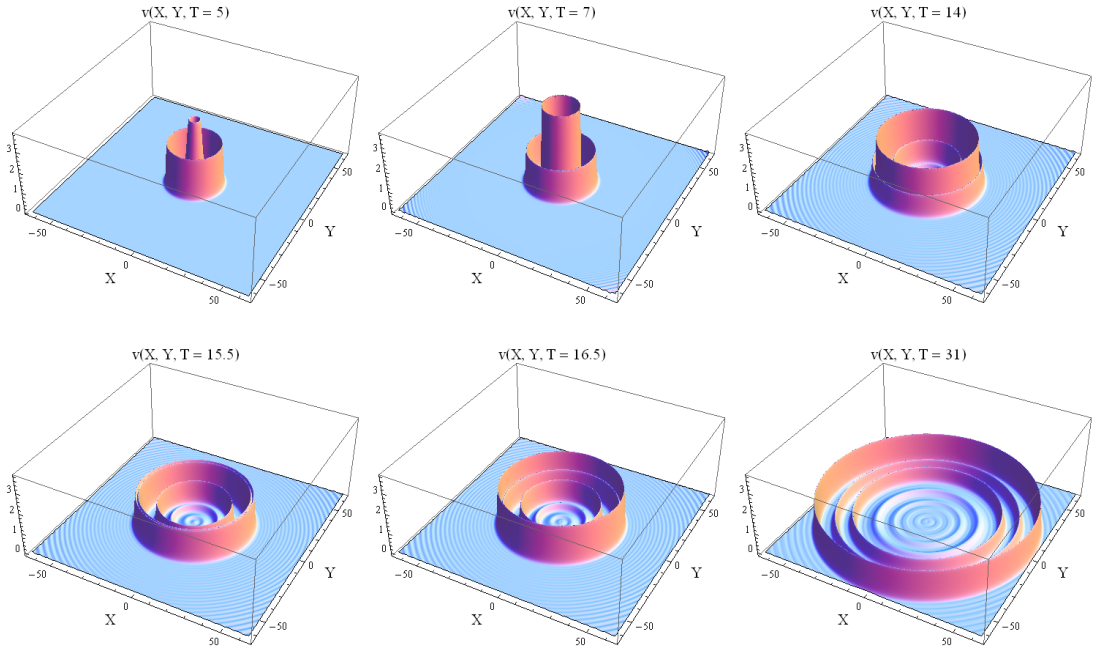


FIG. 26: Numerical ring-type solution of cKdVE, i.e., Eq. (10) in $(X, Y, T)$ domain. The initial condition is fixed according to Eq. (23), where $n = 2$, $u_{m1} = 0.5$, $u_{m2} = 2$, $R_1 = 2$, $R_2 = 15$, and $T_{min} = 5$.

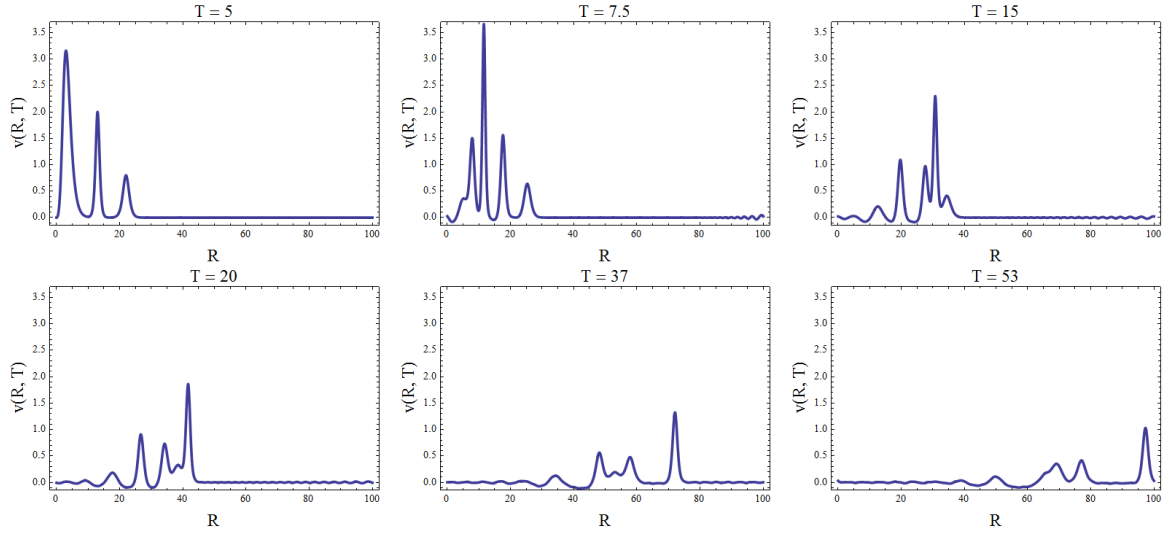


FIG. 27: Elevation $v$ of the numerical solution of cKdVE, i.e., Eq. (10), vs $R$ at fixed values of $T$, satisfying the boundary condition (20). The initial condition is fixed according to Eq. (24), where $n = 2$, $u_{m1} = 0.5$, $u_{m2} = 2$, $u_{m3} = 0.8$, $R_1 = 2$, $R_2 = 13$, $R_3 = 22$, and $T_{min} = 5$.

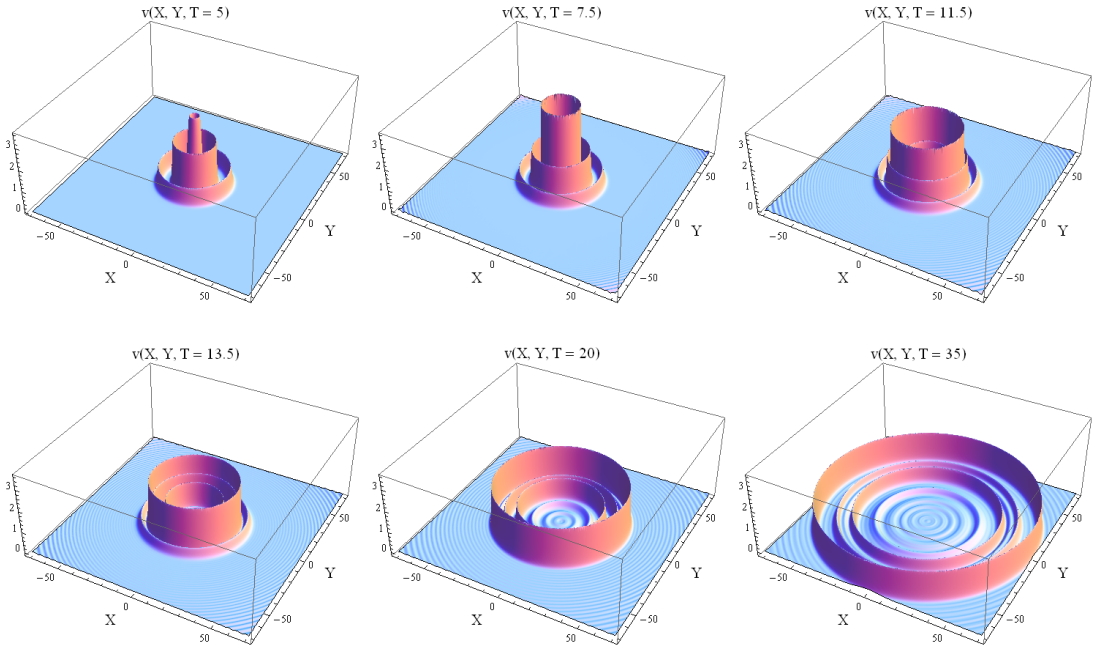


FIG. 28: Numerical ring-type solution of cKdVE, i.e., Eq. (10) in $(X, Y, T)$ domain. The initial condition is fixed according to Eq. (24), where $n = 2$, $u_{m1} = 0.5$, $u_{m2} = 2$, $u_{m3} = 0.8$, $R_1 = 2$, $R_2 = 13$, $R_3 = 22$, and $T_{min} = 5$.

## VI. SUMMARY OF THE NUMERICAL RESULTS: QUALITATIVE ANALYSIS

The results we have obtained in section V are here summarized and discussed.

According to Figures 7 – 28, all our numerical results concern the spatiotemporal evolution of an initially given multi-soliton-like profile of the water wave elevation. In some cases, we have considered one-, two- or three-soliton profiles, while in the others we have chosen the profiles with the form of either a soliton multiplied by a power of $R$, or a linear combinations thereof. In the $(R, T)$ domain, they appear as single- or multi-pulse structures that are propagating to the right, whilst in the $(X, Y, T)$ domain they appear as single- or multi-ring structures propagating outward (divergent rings). For any $T > T_{min}$, these initial structures evolve as the result of their free fall and according to Eq. (10). They exhibit certain nonlinear and dispersive features that are systematized as follows.

The general structure of the numerical solutions during the evolution is basically a multi-

soliton-like packet (i.e., a one-, two-, three- or four-soliton-like structure) which is propagating toward larger values of $R$. In most of the investigated cases, rearwards of such structures, there appears a set of ripples in the form of *water wake*. In the terminology used in the nonlinear wave propagation, one may also refer this effect to as the *radiation* of the soliton-like structure. Generally, as $T$ increases, the amplitudes of the pulses in the initial multi-soliton structure start to decrease gradually, while the *radiation tail* (or the wake) becomes longer, with an increasing number of ripples. In some cases, small ripples appeared ahead of the localized structure, most likely due to the applied periodic boundary conditions. In several cases, the structure featured an internal wave dynamics that might be attributed to the pulse interactions.

### A. Physiological temporal decay of the amplitudes

During the evolution, the amplitude of the water wake appears limited. The amplitudes of the soliton-like pulses decay as $T$ increases, but practically preserving the soliton-like character until their amplitudes was reduced almost to the same order of magnitude of the water wake. Actually, any multi-ring structure exhibits this feature, so that the entire structure decays as $T$ increases. We refer this effect to as the *physiological decay* of the structure. This is an intrinsic geometrical property of our concentric solutions found in cylindrical symmetry.

### B. Complementarity between maximum amplitude and width in a single-pulse

As $T$ increases, the evolution of the packets is accompanied not only by the decrease of the single pulses, but also by their *physiological spreading*, leading to the stage of *packet flattening*. Therefore, as in the analytical tilted multi-ring structures, the physiological decay and the multi-ring spreading manifest as two complementary effects: the greater the amplitude the smaller the width, and vice versa. Furthermore, we have observed that the smaller $T_{min}$ corresponds both to the higher rate of the amplitude decay and to the increase of the width. Such a complementarity is the key of reading for the effect shown in Figures 15 and 16, where the initial profile, after splitting into three secondary pulses (i.e., the breakup effect, see next section VI C), becomes sharper and therefore increases its amplitude (see

section VI D).

### C. Break-up of a single-soliton-like pulse into two or more pulses

Each single-soliton-like pulse, within an initially given multi-soliton structure, that is multiplied by powers of $R$ (such as profiles given in Eqs. (19) or (23) or (24)), breaks up into two or more secondary pulses. Such initial pulse we refer to as the *father pulse*. One of them is dominant in terms of amplitude. We may figure out that the father pulse has been transformed into the dominant secondary pulse after splitting from the smaller secondary pulses. Therefore, it becomes sharper since a part of it has created smaller pulses.

### D. Enhancement of a single-pulse after the break-up

As a consequence of the *maximum amplitude-width complementarity*, during the breakup, those dominant secondary pulses that became sufficiently sharp, undergo an enhancement to amplitudes that considerably exceed the height of the initial father pulse.

### E. Dependence of ring velocity on ring amplitude

We have observed another important feature that relates, similarly to the planar case, the speed of a soliton-like pulse to its maximum amplitude. This can be observed in dynamical situations of multi-ring soliton structures, such as the overcoming of shorter pulses by higher pulses (Figures 11 – 28) or the final arrangement of pulses with respect to increasing amplitude as well as increasing relative separation (i.e., multiplet of ring solitons formation, see Figures 15 and 16). The careful analysis of the above dynamical situations (especially multiplet formation) leads us to the conclusion that the single-ring soliton has a speed that is directly proportional to its maximum amplitude, like in the planar case. This has also been confirmed by the quantitative analysis presented below.

### F. Single-ring solitary structures

For an initial condition corresponding to a single bright soliton (see Figures 7 and 10), we have found a solution whose spatiotemporal evolution does not exhibit the dynamics

corresponding to the break-up of the initial profile. Apart from the physiological decay and spreading, these solutions preserve almost completely the form of their initial profile. They comprise the cylindrical version of the planar bright solitons that preserve their shapes while propagating.

From the qualitative analysis carried out in sections VI A – VI E, we can conclude that the above mentioned features, compared to the ones exhibited by the planar solitary structures, are all ascribed to a soliton-like behaviour of the multi-ring structures that have been examined in this section. In the next sections, we evaluate some of these features from the quantitative point of view.

## VII. QUANTITATIVE ANALYSIS

In the preceding sections, we have clearly shown the existence of laws that relate with each other some of the quantities associated with the ring-type structures, such as physiological decay and spreading, respectively, maximum amplitude-width complementarity, dependence of the ring-soliton speed on the amplitude, break-up, etc. However, the analysis we have carried out is not sufficient to demonstrate those laws quantitatively. Here, on the basis of the numerical data that are extracted from the numerical solutions, we find the temporal law of the physiological decay and spreading, of the amplitude-width complementarity law, and of the dependence of the ring-soliton speed on the amplitude.

The cKdVE (10) has been solved numerically with the boundary condition (20), by fixing the initial condition with Eq. (19) for $n = 0$, $R_0 = 10$, $u_{m0} = 1$ for different $T_{min}$ ranging from 0.01 to 15.

### A. Temporal law of the physiological decay

Figure 29 displays the maximum amplitude $u_m$ during the temporal evolution of the solitary pulse (physiological decay). The dotted plots correspond to the numerical data while the solid lines are the related best fits. It is immediately clear that the rate of the amplitude decay is greater for the smaller $T_{min}$. As $T_{min}$ increases, the decay becomes slower. One can figure out the asymptotic behaviour as the temporal stage that corresponds to an infinitely slow decay which is also predicted analytically by Eq. (10) for $T \to \infty$,

which recovers the pKdVE. According to this prediction, Figure 29 shows that, for fixed $T_{min}$, if $T$ is relatively large, $u_m$ becomes almost constant whilst, if $T$ is relatively small, $u_m$ varies sensitively. Therefore, the early time solitary pulse evolution is more affected by its *cylindrical* character than the longer scale time evolution. All the best fits found for the plot of Figure 29 are described by the following mathematical expression:

$$u_m(T) = q + (u_{m0} - q)\, \exp\left[\beta\left(T^{-1/3} - T_{min}^{-1/3}\right)\right] , \tag{25}$$

where the parameters $q$ and $\beta$ depend on the $T_{min}$.

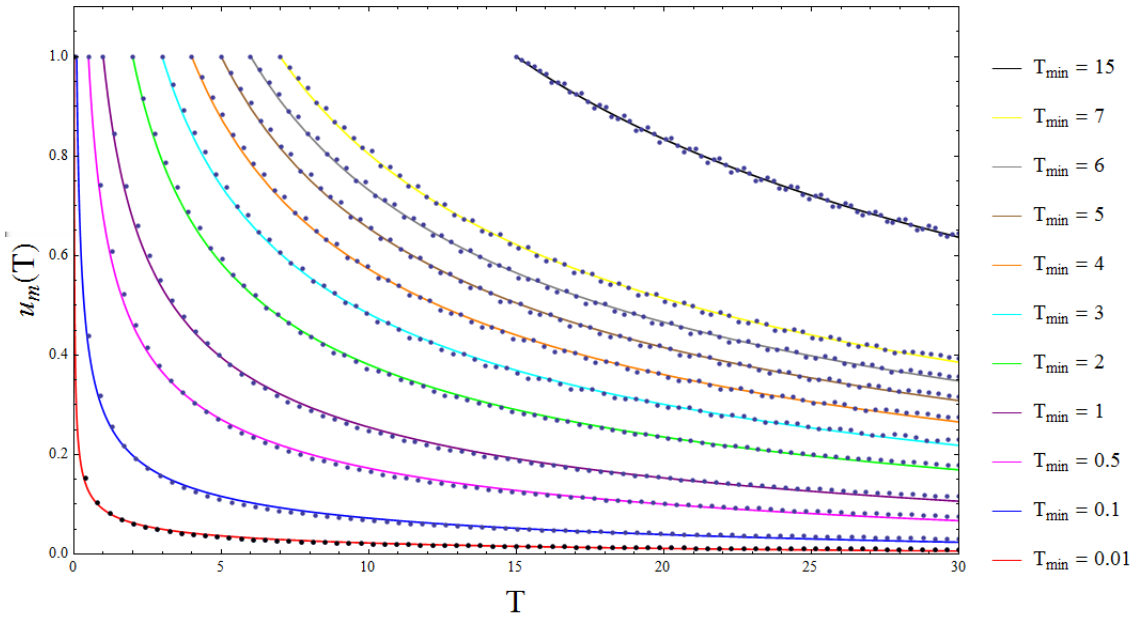


FIG. 29: $u_m$ versus $T$ for different $T_{min}$. The initial profile corresponds to Eq. (19) for $n = 0$, $R_0 = 10$, and $u_{m0} = 1$. Plots from bottom to top correspond to $T_{min}$ ranging from 0.01 to 15.

### B. Temporal law of the physiological spreading

In a similar way, we have determined the values of the soliton pulse width, i.e., $\sigma$, that are plotted in Figure 30 for several values of $T_{min}$ ranging from 0.01 to 15. As for the amplitude, for early times, the evolution of the physiological spreading is strongly affected by the cylindrical character of the numerical solutions. The dots represent the numerical data while the solid lines are the best fits. It has been found that the latter are expressed

by the following general mathematical form:

$$\sigma(T) = \frac{p + \left(\sqrt{\frac{4}{3\,u_{m0}}} - p\right) \exp\left[-\mu\left(T^{-1/3} - T_{min}^{-1/3}\right)\right]}{\alpha + (u_{m0} - \alpha) \exp\left[-\kappa\left(T^{-1/3} - T_{min}^{-1/3}\right)\right]}\,, \tag{26}$$

where the parameters $p$, $\alpha$, $\mu$, and $\kappa$ depend on $T_{min}$.

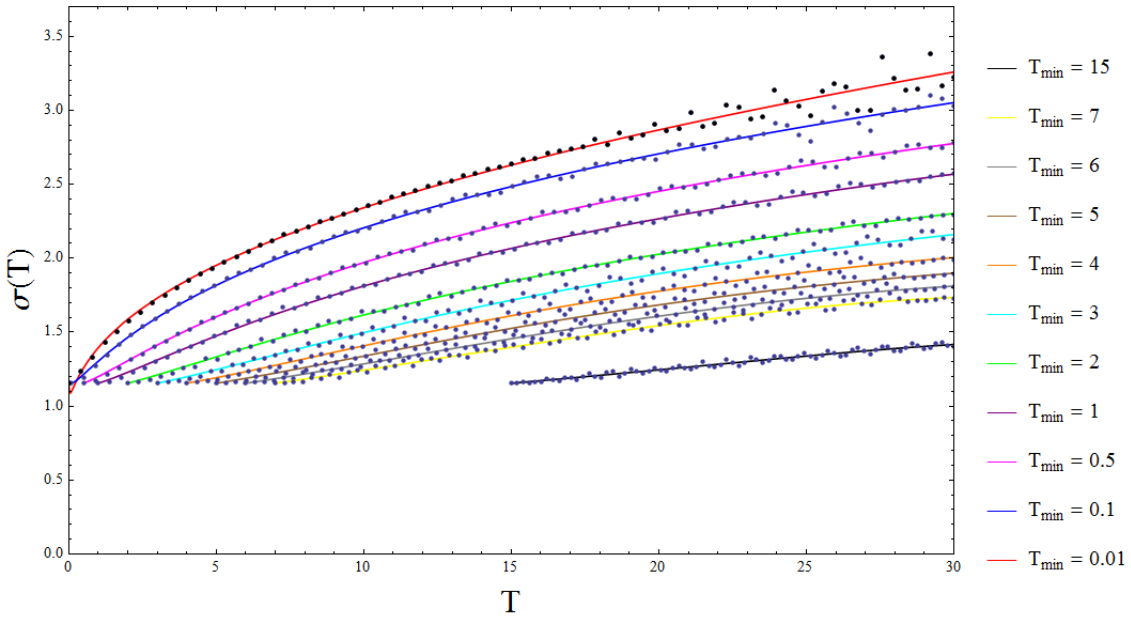


FIG. 30: $\sigma$ versus $T$ for different $T_{min}$. The initial profile corresponds to Eq. (19) for $n = 0$, $R_0 = 10$, and $u_{m0} = 1$. Plots from bottom to top correspond to $T_{min}$ ranging from 0.01 to 15.

### C. Amplitude-width complementarity law

The product $u_m\sigma^2$ has been plotted as a function of $T$ in Figure 31 for different values of $T_{min}$. Dots represent the numerical data while solid lines are the best fits. It is evident that, for sufficiently large $T$, this product becomes independent of $T$. This limit recovers the usual complementarity between $u_m$ and $\sigma$ of the planar case. However, during the early times, roughly, for times not exceeding $T = 10 - 15$, the cylindrical character of the solution is manifested through a violation of the constancy of this product. Of course, for large times the cKdVE reduces to the pKdVE and the constancy of the product is consistent with this limit. It turns out that, according to Figures 29 and 30, $\sigma$ increases when $u_m$ decreases and viceversa $\sigma$ decreases when $u_m$ increases, indicating the complementarity behaviour of these two quantities. Nevertheless, in the cylindrical regime, the complementary variation

of these two functions do not compensate each other as in the planar case. This analysis shows the limits of previous investigations [13, 14] which did not predict the behaviour of the above product when the cylindrical character of the soliton solution is dominant during its evolution. These early works showed only the constancy of the product $\sigma^2 u_m$, which is actually verified for larger times. The best fits found are described by the following mathematical expression:

$$\sigma(T)^2\, u_m(T) = \chi + (4/3 - \chi) \exp\left[\nu \left(T^{-1/3} - T_{min}^{-1/3}\right)\right] , \tag{27}$$

where the parameters $\chi$ and $\nu$ depend on $T_{min}$.

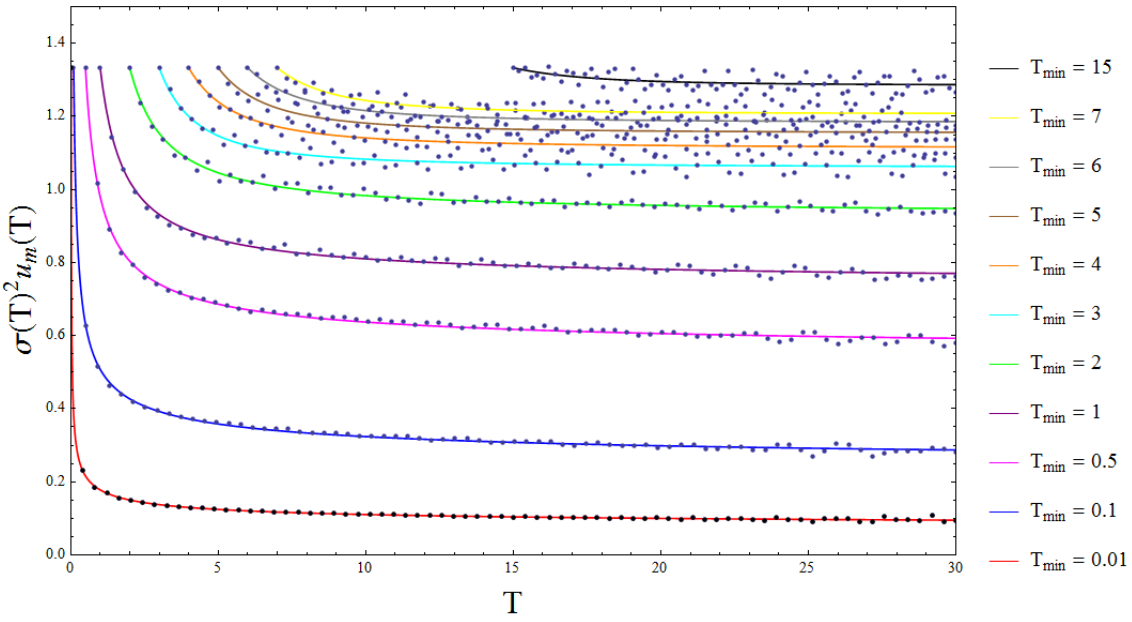


FIG. 31: $u_m\,\sigma^2$ versus $T$ for different $T_{min}$. The initial profile corresponds to Eq. (19) for $n = 0$, $R_0 = 10$, and $u_{m0} = 1$. Plots from bottom to top correspond to $T_{min}$ ranging from 0.01 to 15.

### D. Dependence of the ring-soliton speed on the amplitude

Figure 32 shows the soliton speed $V_0$ versus the initial soliton amplitude $u_{m0}$, during the time evolution of an initially given single-soliton pulse according to Eq. (10) for several initial times $T_{min}$. The dots correspond to the values of $V_0$ that have been obtained from the best fits of the instantaneous position $\overline{R}(T)$ of the soliton centroid (phase shift). The initial soliton profile is peaked around the initial position $R_0 = 10$ [note that $R_0 = \overline{R}(T_{min})$].

We have found that the best fits of $\overline{R}(T)$ at each $T_{min}$ for a given $u_{m0}$ is described by the following relationship:

$$\overline{R}(T) = R_0 + c_0 \left(T - T_{min}\right), \tag{28}$$

where the slope $c_0$ depends on $T_{min}$ and $u_{m0}$ and corresponds to the speed $V_0$, defined as $V_0 = d\overline{R}(T)/dT$. During the time evolution that we explored, for $T_{min}$ ranging from 0.5 to 10, the speed $V_0$ appeared to be independent on time $T$. In Figure 32, we have plotted the correspondence between $V_0$ and $u_{m0}$. The solid lines correspond to the best fits of such a correspondence. For fixed $T_{min}$ (i.e., within each straight line), we have normalized the speeds to their minimum value. The resulting arrangements of the straight lines is shown in Figure 33. We can draw the following conclusions. (i) For a one-soliton solution, there exists a proportionality between the soliton speed and the initial amplitude. (ii) For fixed $T_{min}$, during the evolution, a single-soliton preserves its speed, which is associated with a precise value of the initial amplitude. The instantaneous amplitude experiences a physiological decay, but nevertheless its speed remains unchanged. This is evident from Figure 34, where 3D plots of the numerical solution are displayed in the $(R, T)$ domain. We note that all soliton pulses move along oblique straight lines in the $(R, T)$ domain. This implies that their speed does not change, although their amplitudes decay due to the physiological decay. (iii) For fixed $u_{m0}$, during the evolution, the soliton does not change its speed; for different $T_{min}$, we have different constant speeds. (iv) For fixed $T_{min}$, during the evolution, the soliton does not change the speed, but for different $u_{m0}$ it moves with different constant speed. Therefore, the one-soliton speed is not affected by the physiological change but it changes linearly as the initial amplitudes. This property is ascribed as a typical soliton behaviour and represents an *imprinting* given by $u_{m0}$ to the soliton that exhibits as the constancy of $V_0$.

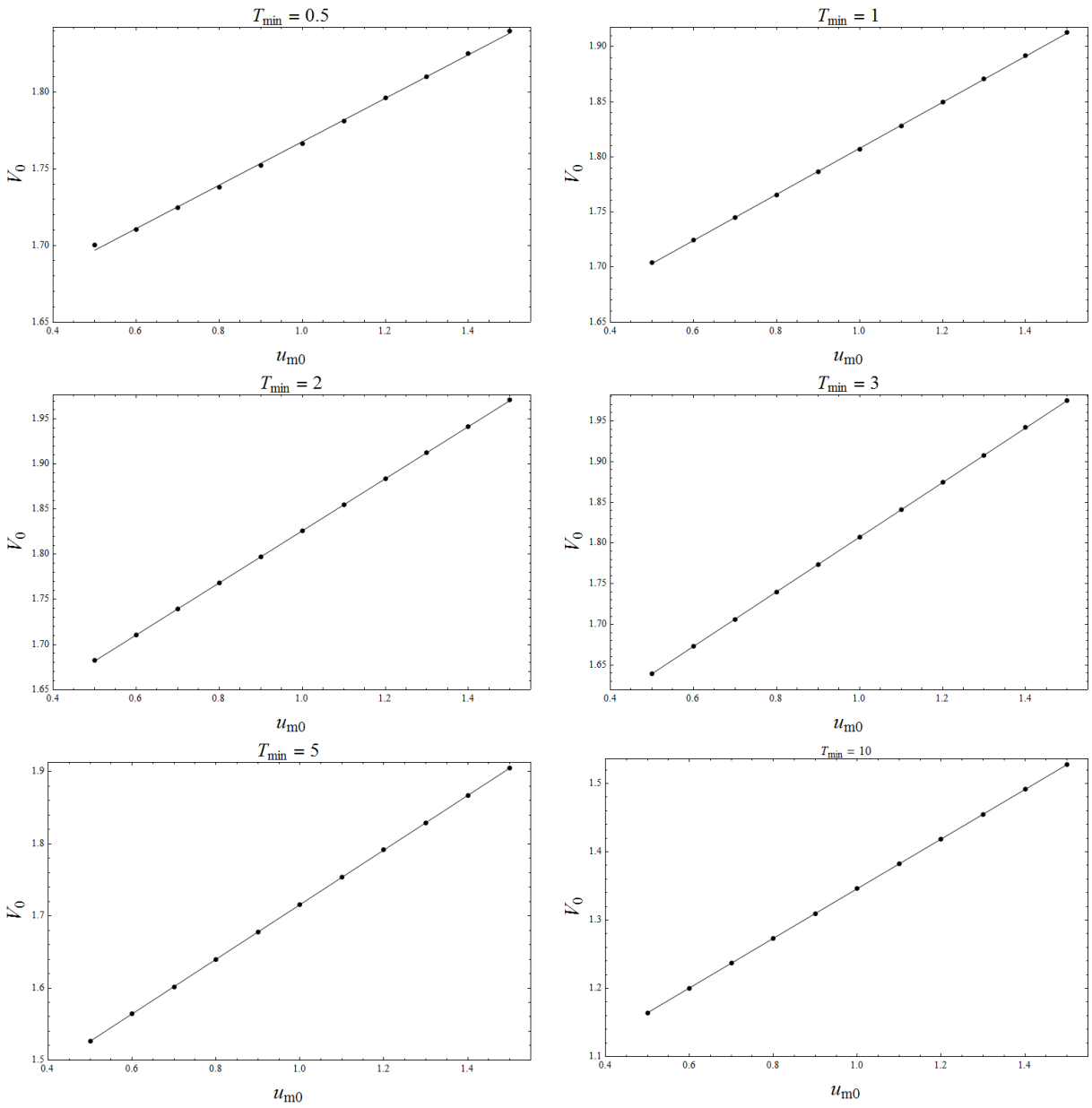


FIG. 32: One-soliton pulse speed, $V_0$, as the function of the initial amplitude $u_{m0}$ for different initial times $T_{min}$. The dots have been obtained by the numerical integration of Eq. (10), with the initial condition Eq. (19).

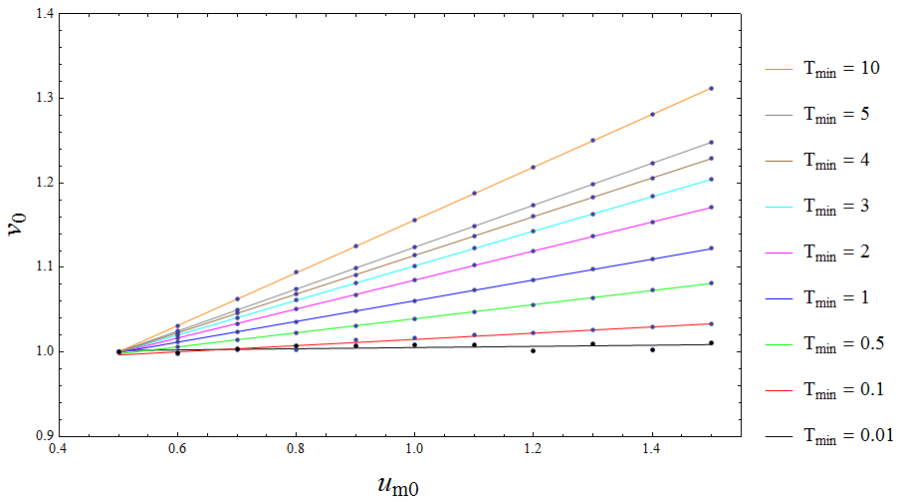


FIG. 33: Normalized one-soliton pulse speed, $v_0$, as the function of the initial amplitude $u_{m0}$ for different initial times $T_{min}$. The normalization of the speeds $V_0$ displayed in Figure 32 have been obtained by dividing them by the minimum speed corresponding to the fixed $T_{min}$. The dots are given by the numerical integration of Eq. (10), with the initial condition Eq. (19).

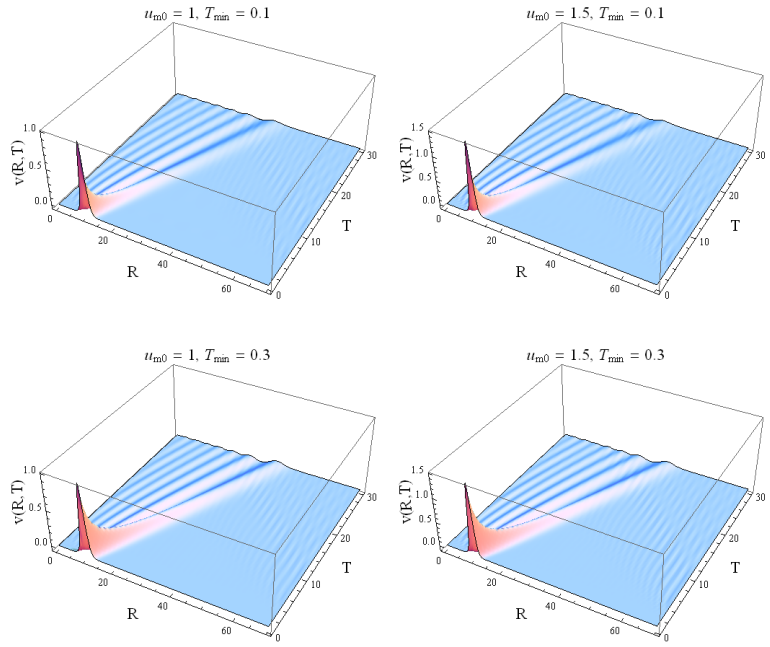


FIG. 34: continued

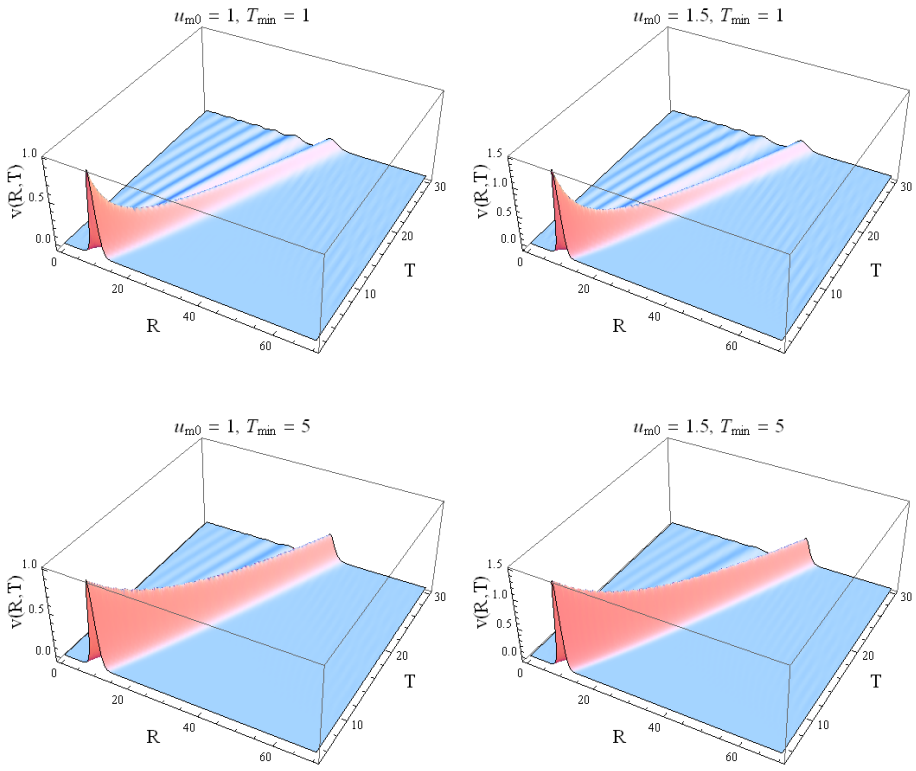


FIG. 34: 3D plots of the numerical solution of cKdVE (10), whose initial condition is given by Eq. (19) in the $(R, T)$ domain, for $n = 0$ and $R_0 = 10$. All soliton pulses move along oblique straight lines in the $(R, T)$ domain and their speed does not change. For fixed $u_{m0}$, the soliton does not change its speed during the evolution, but for different $T_{min}$, we have different constant speeds. For fixed $T_{min}$, the soliton does not change the speed during the evolution, but for different $u_{m0}$ it moves with different constant speed.

## VIII. CONCLUSIONS AND REMARKS

In this work, a theoretical investigation on nonlinear surface gravity waves in the form of ring-type localized waves, in a shallow water, has been carried out within the context of the fluid model that is governed by the set of Euler's fluid equations in cylindrical geometry. We have regarded the water as an incompressible, inviscid, irrotational fluid. In a shallow water, using the method of multiple scales, we have reduced the set of fluid equations to the cKdVE by which we studied, both analytically and numerically, the nonlinear propagation of

cylindrical (or concentric) perturbations in the form of multi-ring solitons. Our investigation can be summarized as follows.

We have demonstrated the existence of exact analytical solutions of the cKdVE in the form of tilted bright multi-ring solitons. To get multi-soliton (one-, two-, and three-soliton) solutions of cKdVE, we have established a one-to-one correspondence that relates cKdVE and pKdVE. Then, analytical tilted soliton solutions of cKdVE have been presented in the $(R, T)$ domain where $R$ and $T$ play the role of the radial- and the time-like variables, respectively. These analytical solutions are also expressed in the form of multi-ring type solitons in the $(X, Y, T)$ domain. We have cast the governing cKdVE in such a way that, in the $(R, T)$ domain, the localized single soliton or multi-soliton structures propagate from the left to the right. In $(X, Y, T)$ domain, the corresponding single- or multi-ring structures propagate outward (divergent rings). These analytical solutions satisfy tilted boundary conditions. Therefore, in the $(R, T)$ domain, they can be thought of as the superposition of a flat, oblique profile and a multi-soliton with standard boundary conditions whilst, in $(X, Y, T)$ domain, they can be thought as the superposition of a conic-shaped water surface and a ring-type multi-solitons satisfying standard boundary conditions. They have been characterized with respect to the presence or absence of properties typically ascribed to a soliton-like behaviour, such as the overlapping of two pulses (i.e., rings), the break-up of a single pulse (i.e. ring) in two or more pulses (rings), the overcoming of one pulse/ring by another one, the amplitude – width complementarity law, the dependence of the soliton speed on the soliton amplitude. We have found that, although these solutions are affected by the physiological temporal variation (i.e., amplitude decrease as $1/T$ and width increase as $T$), the amplitude – width complementarity law is satisfied as in the planar case but instantaneously [i.e., the product $(maximum\ amplitude) \times (width)^2$ is independent of $T$ and fixed by the coefficients of the cKdVE]. However, we have found that other soliton-like properties are not verified. The velocity of these structures is independent of their amplitude and, in addition, the two- and three-soliton structures do not show the effects of the overcoming and overlapping or any other internal dynamics, such as break-up of a single pulse/ring into two or more pulses/rings while moving, and multiplet formation. But, nevertheless, they are the exact transformation of multi-soliton solutions of the pKdVE into solutions of the cKdVE, where each pulse/ring preserves its soliton-like shape for all the time evolution.

We have carried out a detailed numerical analysis of the spatiotemporal evolution, that is governed by the cKdVE, of initially given multi-pulse/ring solitary waves by imposing standard boundary conditions. Similarly to the analysis applied for the tilted analytical solutions, we have attentively characterized the numerical structures during the evolution with respect to the presence or absence of properties typically ascribed to a soliton-like behaviour (i.e., overlapping of two pulses/rings, break-up of a single pulse/ring in two or more pulses/rings and multiplet formation, overcoming of one pulse/ring by another one, the amplitude – width complementarity law, the dependence of the soliton speed on the initial soliton amplitude). We have observed that such structures satisfy all these features. However, they confirm only partially what have been reported by previous pioneering investigations. In particular, the *amplitude – width* complementarity laws is satisfied only for asymptotic times, whilst in the early times (during which the *cylindricality* of the cKdVE is dominant) the complementarity appears in a different form, invoking the violation of the constancy of the product $(maximum\ amplitude) \times (width)^2$. This is due to the different physiological variations of the amplitude and the width compared to the tilted analytical solutions.

Remarkably, the radiation tail (i.e., the water wake) that occurs in every single numerical solution raise a question mark on the stability of the above numerical solutions. Actually, it appears as not growing and constituted by very small ripples behind each multi-pulse structure we have investigated. They appear still stable until times that are sufficiently long to consider the physiological amplitude decay of each pulse to be in the asymptotic conditions. In these asymptotic conditions, each pulse preserves its own soliton-like character but the ripples remain still limited by much smaller values of the amplitude whilst the *cylindricality* of the solution is almost over (as T goes to asymptotic values, the multi-pulse structure reaches the planar form). In conclusion, the radiation tails seem to be not a problem for the stability of the numerical solutions we have investigated. Moreover, according to the qualitative and quantitative analyses carried out in sections VI and VII, some aspects of the instability/stability come into play in those evolution of the multi-pulse structures that exhibit an internal dynamics involving both break-up of initial pulses and/or their overlapping, leading to the multiplet formation. These specific evolutions are the clear manifestation of an unstable initial condition that evolves toward the stability that is represented by the multiplet stage formation. In addition, once this stage is reached, the system is already in the

asymptotic times, but nevertheless the pulses of the multiplet still preserve their solitonic shapes with amplitudes that are much greater than the ones of the radiation tails which indeed appear stable.

To conclude this section, we want also to put forward a discussion on the possible reproducibility of the tilted solitons that have been predicted in this manuscript. To this end, suitable convex bodies can be employed. They should be shaped according to a conical form, with the height much less than $h_0$ and the base diameter much greater than $h_0$, and with one or more ring-soliton-shaped concave annular protrusions on the lateral surface. They should be placed on the surface of the water and subjected to a push down and then quickly removed from the water. In this way, both the initial and boundary conditions are the ones corresponding to Figures 1 - 6. So that, with ordinary equipment used to study artificially-generated water waves, one can carry out the suitable measurements to compare the theoretical predictions with the experimental observations. In a future work, we expect to report on satisfactory results concerning this comparison. Of course, in the exact analytical solutions, the bending of the surface of the water would extend to infinitely large radial distance, whilst in the reality the bending experimentally/artificially produced becomes flat after a relatively long distance compared to $h_0$. It is obvious that, once generated, the conical-shaped surface evolves in time toward the asymptotic condition in which, to preserve the volume of the water, the ring waves, while propagating, experience the physiological decay of their amplitude and the tilted surface becomes progressively horizontal showing the flattening of the initial soliton rings.

## Appendix A: Derivation of the cylindrical KdVE

To derive the cylindrical Korteweg-de Vries equation (cKdVE), we follow Refs. [6, 17, 25]. We introduce the stretched coordinates, $\zeta$ and $s$, and the new variables $H$, $P$, $U$, $W$, respectively, i.e.

$$\zeta = \frac{\epsilon^2}{\delta^2}(r-t), \quad s = \frac{\epsilon^6}{\delta^4}r, \quad (\eta, p, u_r) = \frac{\epsilon^3}{\delta^2}(H, P, U), \quad w = \frac{\epsilon^5}{\delta^4}W\,, \tag{A1}$$

Equations (1) – (5) become

$$-\frac{\partial U}{\partial \zeta}+\gamma\left(U\frac{\partial U}{\partial \zeta}+W\frac{\partial U}{\partial z}+\gamma U\frac{\partial U}{\partial s}\right)=-\left(\frac{\partial P}{\partial \zeta}+\gamma\frac{\partial P}{\partial s}\right), \tag{A2}$$

$$\gamma\left[-\frac{\partial W}{\partial \zeta}+\gamma\left(U\frac{\partial W}{\partial \zeta}+W\frac{\partial W}{\partial z}+\gamma U\frac{\partial W}{\partial s}\right)\right]=-\frac{\partial P}{\partial z}, \tag{A3}$$

$$\frac{\partial U}{\partial \zeta}+\frac{\partial W}{\partial z}+\gamma\left(\frac{\partial U}{\partial s}+\frac{U}{s}\right)=0, \tag{A4}$$

$$P=H \text{ and } W=-\frac{\partial H}{\partial \zeta}+\gamma\left(U\frac{\partial H}{\partial \zeta}+\gamma U\frac{\partial H}{\partial s}\right) \text{ on } z=1+\gamma H \tag{A5}$$

$$W=0 \quad \text{on} \quad z=0, \tag{A6}$$

where we have introduced the new parameter $\gamma=\epsilon^4/\delta^2$. In the shallow water regime (i.e. when $\gamma$ is a small parameter), we seek a solution in the following Taylor expansion form:

$$N\sim\sum_{n=0}^{\infty}\gamma^n N_n, \quad \gamma\to 0,$$

where $N=H,P,U$, and $W$. To compute higher order corrections, the surface boundary conditions at $z=1+\gamma H$ are expressed at $z=1$ by taking the Taylor expansions of $P$, $W$, and $U$ around $z=1$, viz.

$$P_0+\gamma H_0\frac{\partial P_0}{\partial z}+\gamma P_1=H_0+\gamma H_1+O(\gamma^2) \text{ on } z=1 \tag{A7}$$

$$W_0+\gamma H_0\frac{\partial W_0}{\partial z}+\gamma W_1=-\frac{\partial H_0}{\partial \zeta}-\gamma\frac{\partial H_1}{\partial \zeta}+\gamma U_0\frac{\partial H_0}{\partial \zeta}+O(\gamma^2) \text{ on } z=1\,. \tag{A8}$$

To the lowest order in $\gamma$, we get

$$P_0=H_0\,,\ U_0=H_0\,,\ W_0=-z\frac{\partial H_0}{\partial \xi}\,,\ 0\le z\le 1\,,$$

while to the next higher order in $\gamma$, we have

$$-\frac{\partial U_1}{\partial \zeta}+U_0\frac{\partial U_0}{\partial \zeta}+W_0\frac{\partial U_0}{\partial z}=-\frac{\partial P_1}{\partial \zeta}-\frac{\partial P_0}{\partial s}\,, \tag{A9}$$

$$-\frac{\partial W_0}{\partial \zeta}=-\frac{\partial P_1}{\partial z}\,, \tag{A10}$$

$$\frac{\partial U_1}{\partial \zeta}+\frac{\partial W_1}{\partial z}+\frac{\partial U_0}{\partial s}+\frac{1}{s}U_0=0\,, \tag{A11}$$

$$P_1+H_0\frac{\partial P_0}{\partial z}=H_1\,,\ \text{on } z=1 \tag{A12}$$

$$W_1+H_0\frac{\partial W_0}{\partial z}=-\frac{\partial H_1}{\partial \zeta}+U_0\frac{\partial H_0}{\partial \zeta}\,,\ \text{on } z=1 \tag{A13}$$

$$W_1=0\,,\ \text{on } z=0\,. \tag{A14}$$

After combining Eqs. (A10) and (A12), we get the following expression

$$P_1 = \frac{1}{2}(1-z^2)\,\frac{\partial^2 H_0}{\partial \zeta^2} + H_1\,, \tag{A15}$$

and from Eqs. (A9), (A11), and (A15), we obtain

$$W_1 = -\left(\frac{\partial H_1}{\partial \zeta} + \frac{1}{2}\,\frac{\partial^3 H_0}{\partial \zeta^3} + H_0\frac{\partial H_0}{\partial \zeta} + 2\frac{\partial H_0}{\partial s} + \frac{1}{s}\,H_0\right) z + \frac{1}{6}\,z^3\,\frac{\partial^3 H_0}{\partial \zeta^3}\,. \tag{A16}$$

The latter satisfies the impermeable bed condition and the surface boundary condition on $z = 1$ yields

$$W_1 = -\left(\frac{\partial H_1}{\partial \zeta} + \frac{1}{2}\,\frac{\partial^3 H_0}{\partial \zeta^3} + H_0\frac{\partial H_0}{\partial \zeta} + 2\frac{\partial H_0}{\partial s} + \frac{1}{s}\,H_0\right) + \frac{1}{6}\,\frac{\partial^3 H_0}{\partial \zeta^3}\,, \tag{A17}$$

while Eq. (A13) gives

$$W_1 = -\frac{\partial H_1}{\partial \zeta} + 2H_0\frac{\partial H_0}{\partial \zeta}\,. \tag{A18}$$

By combining Eqs. (A17) and (A18), we finally obtain the following equation for the leading-order term of the expansion for $H$, i.e., $H_0$:

$$\frac{\partial H_0}{\partial s} + \frac{3}{2}H_0\frac{\partial H_0}{\partial \zeta} + \frac{1}{6}\frac{\partial^3 H_0}{\partial \zeta^3} + \frac{H_0}{2s} = 0\,, \tag{A19}$$

where $\zeta$ and $s$ are the dimensionless stretched space-like and time-like variables, respectively, and the quantity $H_0$ is the rescaled leading order term of the elevation expansion, say $\eta_0$ (for details see Ref. [17]). Equation (A19) is usually referred to as the cylindrical (or concentric) Korteweg-de Vries equation (cKdVE).

---


[1] G.B. Witham, *Linear and nonlinear waves* (John Wiley, New York, 1974).

[2] F. Calogero and A. Degasperis, *Spectral transform and solitons* (North-Holland, Amsterdam, 1982), vol. I.

[3] R. K. Dodd, J. C. Eilbeck, J. D. Gibbon and H. C. Morris, *Soliton and nonlinear wave equations* (Academic Press, London, 1982).

[4] V. I. Karpman, *Nonlinear Waves in Dispersive Media* (Pergamon Press, Oxford, 1975).

[5] C. Sulem and P. L. Sulem, *The Nonlinear Schrödinger Equation: Self-focusing and Wave Collapse* (Springer, New York, 1999).

[6] R. S. Johnson, J. Nonlinear Math. Phys. **10**, 72 (2003).

[7] A. R. Osborne, *Nonlinear Ocean Waves and the Inverse Scattering Transform* (Academic Press, Amsterdam, 2010).

[8] J. Nott, *Extreme Events: A Physical Reconstruction and Risk Assessment* (Cambridge University Press, Cambridge, 2006).

[9] M. Onorato *et al.*, *Physics Reports* **528**, 47 (2013).

[10] C. Kharif, E. Pelinovsky and A. Slunyaev, *Rogue Waves in the Ocean* (Springer, New York, 2009).

[11] C.E. Synolakis and E.N. Bernard, *Phil. Trans. R. Soc. A* **364**, 2231 (2006).

[12] D.C. Giancoli, *Physics for scientists and engineers with modern physics* (Upper Saddle River, N.J., Pearson Prentice Hall, 2000) 4th edition.

[13] S. Maxon and J. Viecelli, Phys. Fluids **17**, 1614 (1974).

[14] S. Maxon, Phys. Fluids **19**, 266 (1976).

[15] F. Calogero and A. Degasperis, Lett. Nuovo Cimento **23**, 150 (1978).

[16] A. Nakamura and H.-H. Chen, J. Phys. Soc. Jpn. **50**, 711 (1981).

[17] R. S. Johnson, *A Modern Introduction to the Mathematical Theory of Water Waves* (Cambridge University Press, Cambridge, 1997).

[18] R. Hirota, Phys. Lett A **71**, 393 (1979).

[19] R. Fedele, S. De Nicola, D. Grecu, P. K. Shukla, and A. Visinescu, AIP Conf. Proc., **1061**, 273 (2008).

[20] R. Fedele, S. De Nicola, D. Grecu, A. Visinescu, and P. K. Shukla, AIP Conf. Proc., **1188**, 365 (2009).

[21] F. Calogero and A. Degasperis, Lett. Nuovo Cimento **28**, 12 (1980).

[22] G. P. Leclert, Ch. F. F. Kharney, A. Bers, and D. J. Kaup, Phys. Fluids **22**, 1545 (1979).

[23] P. Carbonaro, R. Floris, and P. Pantano, Il Nuovo Cimento **6C**, 133 (1983).

[24] A. D. Polyanin and V.F. Zaitsev, *Handbook of nonlinear partial differential equations* (CRC Press, New York, 2012) 2nd edition.

[25] R. S. Johnson, J. Nonlinear Math. Phys. **19**, 1240012 (2012).

[26] K. R. Khusnutdinova, C. Klein, V. B. Matveev and A. O. Smirnov, *Chaos* **23**, 013126 (2013).